alization after orthotopic intestinal neobladder creation. J Urol **163** : 1108-1111, 2000
9) Madersbacher S, Schmidt J, Eberle JM, et al : Long-term outcome of ileal conduit diversion. J Urol **169** : 985-990, 2003
10) Nieh PT : The Kock pouch urinary reservoir. Urol Clin North Am **24** : 755-772, 1997
11) Tobisu K, Tanaka Y, Mizutani T, et al : Transitional cell carcinoma of the urethra in men following cystectomy for bladder cancer : multivariate analysis for risk factors. J Urol **146** : 1551-1553, 1991
12) Lebret T, Herve JM, Barre P, et al : Urethral recurrence of transitional cell carcinoma of the bladder. Predictive value of preoperative latero-montanal biopsies and urethral frozen sections during prostatocystectomy. Eur Urol **33** : 170-174, 1998
13) Freeman JA, Tarter TA, Esrig D, et al : Urethral recurrence in patients with orthotopic ileal neobladders. J Urol **156** : 1615-1619, 1996
14) Le Duc A, Camey M and Teillac P : An original antireflux ureteroileal implantation technique : long-term followup. J Urol **137** : 1156-1158, 1987

Original Report

Ukihide Tateishi[1]
Tadashi Hasegawa[2]
Hiroaki Onaya[1]
Mitsuo Satake[1]
Yasuaki Arai[1]
Noriyuki Moriyama[1]

Myxoinflammatory Fibroblastic Sarcoma: MR Appearance and Pathologic Correlation

OBJECTIVE. The purpose of our study was to define the MR appearance of myxoinflammatory fibroblastic sarcoma of the soft tissues and to make correlations with the histopathologic features.

CONCLUSION. Myxoinflammatory fibroblastic sarcoma is an uncommon malignancy that typically affects adult subjects, who present with painless swelling. This lesion manifests on MR images as a poorly circumscribed mass involving the underlying tendon sheath in the distal extremities.

Myxoinflammatory fibroblastic sarcoma of the soft tissues is a rare low-grade tumor of uncertain origin that usually arises in the hands and feet. Myxoinflammatory fibroblastic sarcoma was first described in 1998 by Meis-Kindblom and Kindblom [1]. Montgomery et al. [2] named the tumor "inflammatory myxohyaline tumor" of the distal extremities with virocyte or Reed-Sternberg-like cells. Histologic characteristics are the spindle to epithelioid neoplastic cells as the manifestation of malignancy admixed with the myxoid and hyalinized matrix, the inflammatory infiltrate, and bizarre virocyte or Reed-Sternberg-like cells with enlarged vesicular nuclei [1–3].

More than 100 cases of myxoinflammatory fibroblastic sarcoma have been reported, with a large series identified in two articles [1–6]. However, MRI findings of myxoinflammatory fibroblastic sarcoma have rarely been documented. The purpose of this study was to characterize the MR appearance of myxoinflammatory fibroblastic sarcoma and to correlate that appearance with the histopathologic features.

Materials and Methods

MR images of all patients with pathologically proven myxoinflammatory fibroblastic sarcoma at our institution were retrospectively reviewed. Our institutional review board gave its approval for a review of patient records and images. The patients were identified by review of our institution's pathology database for a 2-year period. The affected patients included three males and one female who ranged in age from 15 to 62 years old (mean age, 35 years). All histopathologic specimens were reviewed by an experienced pathologist to confirm the diagnosis. Histopathologic examination in all patients showed spindle and epithelioid tumor cells with mild nuclear atypia. Ganglionlike cells and Reed-Sternberg-like cells were also prominent in all cases. Inflammatory cells, including neutrophils, lymphocytes, and eosinophils, were densely present in all cases. Immunohistochemistry was performed in all patients, and all tumors displayed immunoreactivity to vimentin, smooth-muscle actin, and CD34. These histopathologic characteristics were compatible with the diagnosis of myxoinflammatory fibroblastic sarcoma [7]. Medical records were reviewed by one of the authors for presenting complaints, disease progression, and outcome. Radiographs, available for all patients, were also evaluated by two radiologists for the presence of soft-tissue masses or nodules, mineralization, and bone destruction. The findings were recorded by consensus.

T1- and T2-weighted MR images were obtained in the sagittal and coronal planes using a surface coil. T1-weighted conventional spin-echo MR images were obtained using a 20-cm field of view, 3.5- to 5-mm section thickness, TR range/TE of 450–520/15, 160 × 256 matrix, and 2 signals acquired. T2-weighted fast spin-echo acquisitions with ($n = 3$) or without ($n = 1$) fat suppression were performed using a 20-cm field of view, 3.5- to 5-mm section thickness, 3,600–4,000/120, 160 × 256 ma-

Received June 2, 2004; accepted after revision July 28, 2004.

Supported in part by grant for Scientific Research Expenses for Health and Welfare Programs, The Foundation for the Promotion of Cancer Research, and second-term Comprehensive 10-year Strategy for Cancer Control.

[1]Division of Diagnostic Radiology, National Cancer Center Hospital and Institute, Tsukiji, Chuo-Ku, 104-0045, Tokyo, Japan. Address correspondence to U. Tateishi.

[2]Pathology Division, National Cancer Center Hospital and Institute, Tsukiji, Tokyo, Japan.

AJR 2005;184:1749–1753

0361–803X/05/1846–1749

trix, and 2 signals acquired. After the IV administration of 0.1 mmol of gadopentetate dimeglumine (Magnevist, Schering) per kilogram of body weight, transverse T1-weighted images with ($n = 3$) or without ($n = 1$) fat suppression were obtained in the sagittal and coronal planes.

MR images were reviewed by two radiologists and findings were recorded by consensus. Images were evaluated for lesion location and size, depth (superficial or deep), shape of margin (well or ill defined), and the presence or absence of extracompartmental extension. To define depth, superficial lesions did not involve the superficial fascia, and deep lesions were deep in relation to or invaded the superficial fascia. The relationship between tumor and the underlying tendon sheath was also evaluated. MR images were evaluated for predominant signal intensity characteristics (low, intermediate, high), signal homogeneity or heterogeneity, and enhancement characteristics. On T1-weighted images, low signal intensity was defined as signal intensity less than that of muscle; intermediate signal intensity, similar to that of muscle; and high signal intensity, similar to that of fat. On T2-weighted images, low signal intensity was defined as signal intensity similar to that of muscle; intermediate signal intensity, greater than that of muscle but less than that of fat; and high signal intensity, equal to or greater than that of fat. Tumor enhancement was visually graded as greater than, less than, or equal to that of surrounding muscle and vessels.

Results

Clinical Features

All patients were symptomatic at presentation. Presenting complaints were painless swelling of the distal extremities. The mean symptom duration was 4.8 months. Tumors arose from the feet ($n = 2$), hands ($n = 1$), and fingers ($n = 1$). All patients received excisional biopsy for definitive diagnosis and primary therapy. Surgical margins were adequate in three patients and inadequate in one patient. The one patient with an inadequate surgical margin underwent subsequent wide resection. Chemotherapy and radiation therapy were not included in the treatment regimen in any patient. Local recurrence occurred 26.5 months after the initial surgery in two patients. These patients received wide resection. At the latest follow-up (27–82 months; mean, 45 months), no patients had developed further recurrence or metastasis.

MRI Findings and Pathologic Correlations

The gross characteristics of the resected specimens featured multinodular architecture corresponding to MRI features. The mean tumor diameter was 2.4 cm (range, 1.2–3.0 cm). Tumors were located along the tendon sheath in all patients. Findings of extensive involvement surrounding the tendon sheath by the tumor were seen. In two patients, the tumor existed beneath the tendon sheath (Fig. 1), and in two it involved the surrounding tendon sheath diffusely and focally infiltrated the dermis (Fig. 2). One patient had an ill-defined, irregularly marginated mass involving the ulnar nerve and the tendon sheath of the flexor carpi ulnaris (Fig. 2).

Cortical invasion was not identified in any patient on radiographs. All tumors showed predominantly low signal intensity relative to muscle on T1-weighted MR images (Fig. 3). Two lesions showed moderate and homogeneous enhancement after the IV administration of contrast material (Figs. 1 and 3). The cut surface of resected specimens showed solid nests of neoplastic cells that featured spindle and epithelioid cells with higher cellularity, which corresponded to homogeneous enhancement on contrast-enhanced MR images. Two lesions showed heterogeneous enhancement of the tumor that correlated with geographic areas of the myxoid stromal matrix on microscopic observations (Fig. 4). On T2-weighted MR images, all lesions had intermediate signal intensity greater than that of muscle but less than that of fat (Fig. 2). In all cases, the cut surface of specimens revealed solid nests of cellular areas with foci of hyalinized collagen fibers and hypocellular areas with a myxoid stromal

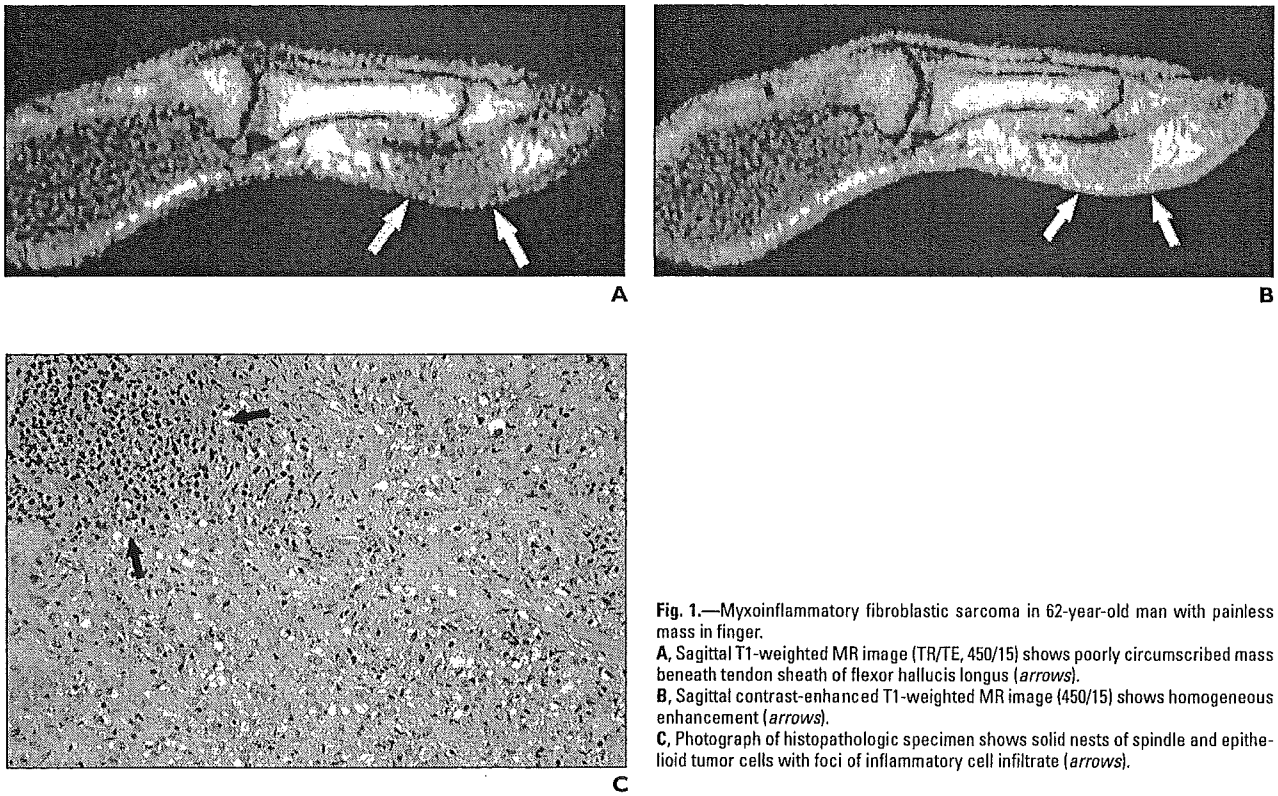

Fig. 1.—Myxoinflammatory fibroblastic sarcoma in 62-year-old man with painless mass in finger.
A, Sagittal T1-weighted MR image (TR/TE, 450/15) shows poorly circumscribed mass beneath tendon sheath of flexor hallucis longus (*arrows*).
B, Sagittal contrast-enhanced T1-weighted MR image (450/15) shows homogeneous enhancement (*arrows*).
C, Photograph of histopathologic specimen shows solid nests of spindle and epithelioid tumor cells with foci of inflammatory cell infiltrate (*arrows*).

matrix, which corresponded to the imaging appearance of intermediate signal intensity on T2-weighted MR images.

Two patients developed recurrent tumors and underwent follow-up MRI after treatment. One patient developed a mass of sheetlike appearance beneath the dorsal portion of the underlying tendon sheath (Fig. 3). Signal characteristics and homogeneous enhancement patterns were similar to those of the primary tumors. Histopathologic examination of this patient showed an infiltrate of lymphoid cells and a marked proliferation of spindle-shaped tumor cells surrounding the tendon sheaths.

In the second patient, a mass of branching pattern occurred along the extensor digitorum longus tendon sheaths of the second and fourth toes without distortion of the architecture of the tendon sheaths (Fig. 4). This patient had also MRI findings suggesting capsular involvement in the metatarsophalangeal joint of the second toe. Histopathologic examination revealed that the tumor arose from the extensor digitorum longus tendon sheaths and also involved the extensor digitorum brevis tendon sheath, cutaneous nerve, and dermis.

Discussion

Myxoinflammatory fibroblastic sarcoma is a rare tumor of the subcutaneous soft tissue that can arise on the trunk but most commonly occurs in the distant extremities [1, 2]. According to the literature and our experience, myxoinflammatory fibroblastic sarcoma is a tumor that most commonly affects adults who are symptomatic at presentation [1, 2]. All patients in our series were symptomatic, with common complaints of a painless mass.

Myxoinflammatory fibroblastic sarcoma has a relatively good prognosis with a long life expectancy despite frequent local recurrence [1–3]. Two of our patients developed local recurrence, with an average duration of 26.5 months. According to the literature, the local recurrence rate in patients with myxoinflammatory fibroblastic sarcoma ranges from 22% to 67% [1, 2]. The metastasis rate in patients with myxoinflammatory fibroblastic sarcoma is uncertain. Metastases have been reported to develop in only a few cases [1].

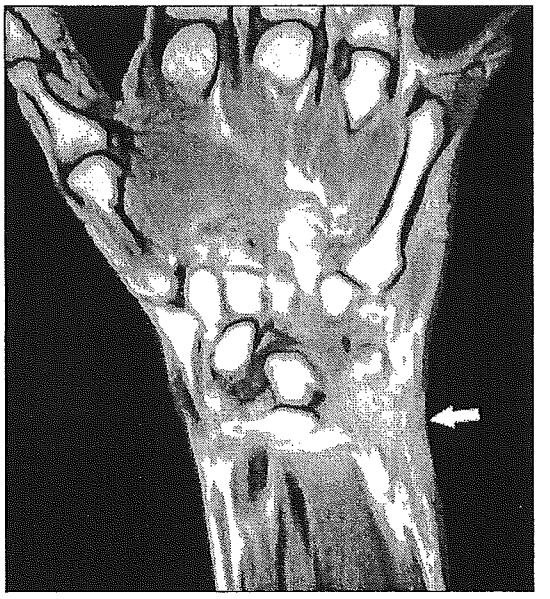

A

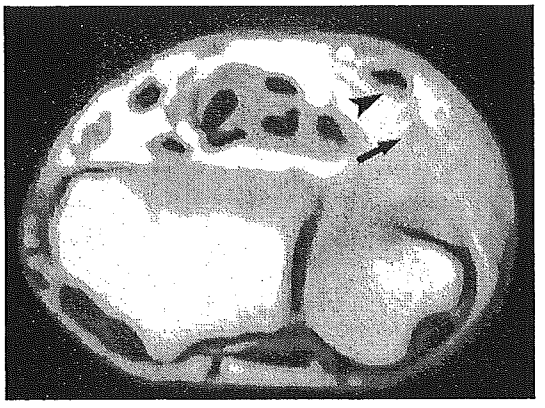

B

C

Fig. 2.—Myxoinflammatory fibroblastic sarcoma in 31-year-old man with painless mass in subcutaneous soft tissue of wrist.
A, Coronal contrast-enhanced T1-weighted MR image (TR/TE, 520/15) shows poorly circumscribed mass with ill-defined border. Tumor involves surrounding tendon sheath diffusely and focally infiltrates dermis (*arrow*).
B, Axial contrast-enhanced T1-weighted MR image (520/15) shows mass involving ulnar nerve (*arrow*) and tendon sheath of flexor carpi ulnaris (*arrowhead*).
C, Photograph of histopathologic specimen reveals that numerous small nodules consisting of tumor cells infiltrate along ulnar nerve (*arrows*).

In all of our patients, excisional biopsy for definitive diagnosis and primary therapy was performed. However, tumor margins in one of our patients were inadequate and the patient underwent subsequent wide resection. Tumors are often removed piecemeal by surgical procedures, with curative wide resection considered to be the adequate treatment of choice [1].

Grossly, myxoinflammatory fibroblastic sarcoma forms a poorly circumscribed mass surrounding the tendon sheath that may extend into the dermis and skeletal muscle. Microscopically, the tumor is characterized by solid nests of atypical spindle and epithelioid cells in a myxoid stroma and dense inflammatory infiltrates. The tumor cells often have large vesicular nuclei similar to those of virocytes or Reed-Sternberg cells. The immunophenotype is positive for vimentin, with variable immunoreactivity for CD34, CD68, cytokeratin, and smooth-muscle actin [1–6].

On MR images, myxoinflammatory fibroblastic sarcoma typically manifests as a poorly circumscribed mass with a multinodular appearance. Extensive involvement surrounding the tendon sheath is also a common feature.

The appearance of the extension along the tendon sheath in this tumor is similar to that seen in tenosynovitis. Differentiating tenosynovitis from myxoinflammatory fibroblastic sarcoma solely on MRI findings is difficult. Tenosynovitis also can lead to an ill-defined soft-tissue mass or enlargement of its sheath. However, this condition typically manifests as the accumulation of fluid with increased signal intensity of the affected tendon on T2-weighted MR images [8]. Clinical characteristics can allow the differentiation of tenosynovitis from myxoinflammatory fibroblastic sarcoma because tenosynovitis often decreases in size during the course of disease, whereas myxoinflammatory fibroblastic sarcoma usually grows with infiltration [1].

MRI findings of myxoinflammatory fibroblastic sarcoma also closely resemble those of giant cell tumors of the tendon sheath, proliferative fasciitis, acral fibromyxoma, myxoid

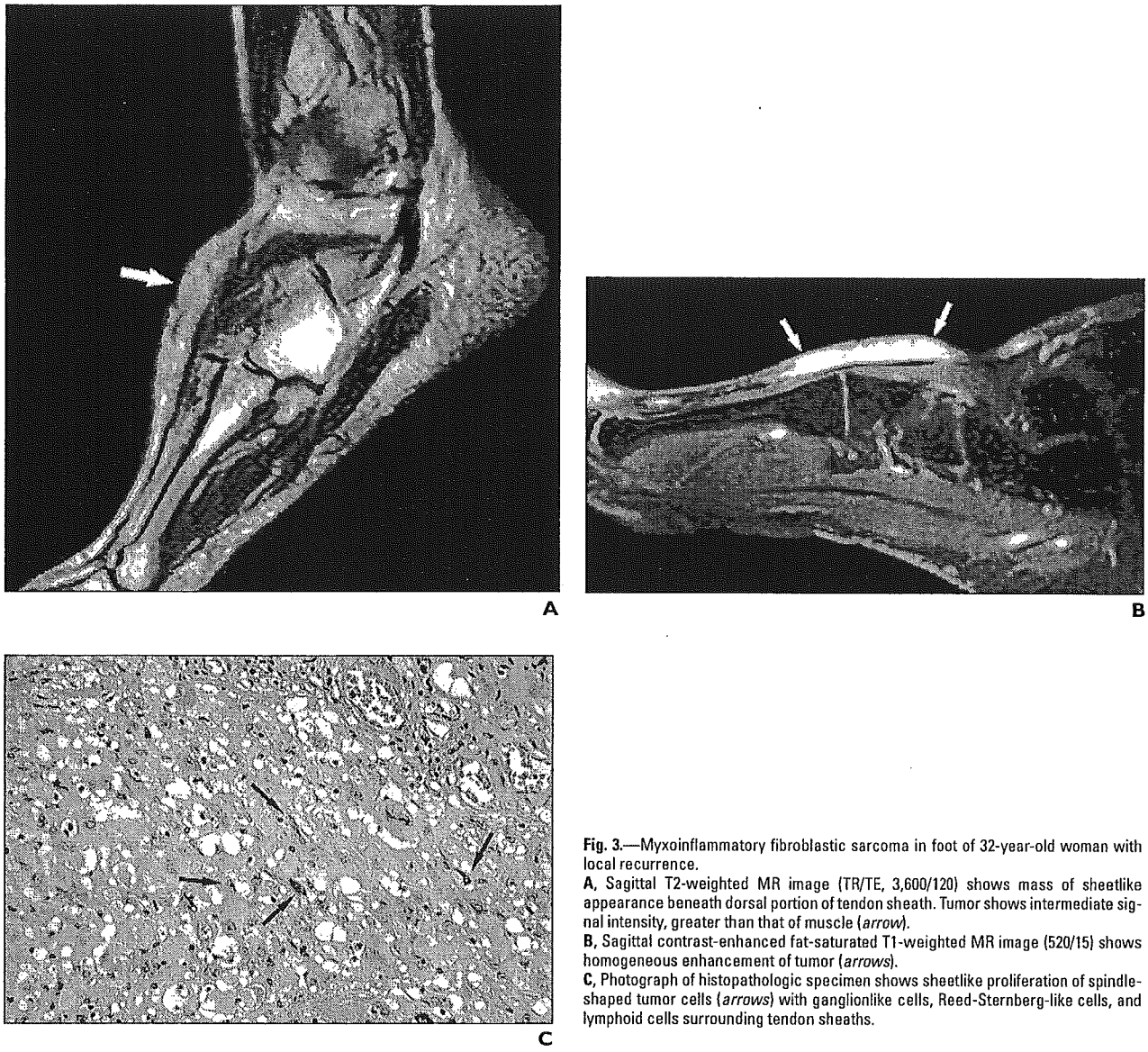

Fig. 3.—Myxoinflammatory fibroblastic sarcoma in foot of 32-year-old woman with local recurrence.
A, Sagittal T2-weighted MR image (TR/TE, 3,600/120) shows mass of sheetlike appearance beneath dorsal portion of tendon sheath. Tumor shows intermediate signal intensity, greater than that of muscle (*arrow*).
B, Sagittal contrast-enhanced fat-saturated T1-weighted MR image (520/15) shows homogeneous enhancement of tumor (*arrows*).
C, Photograph of histopathologic specimen shows sheetlike proliferation of spindle-shaped tumor cells (*arrows*) with ganglionlike cells, Reed-Sternberg-like cells, and lymphoid cells surrounding tendon sheaths.

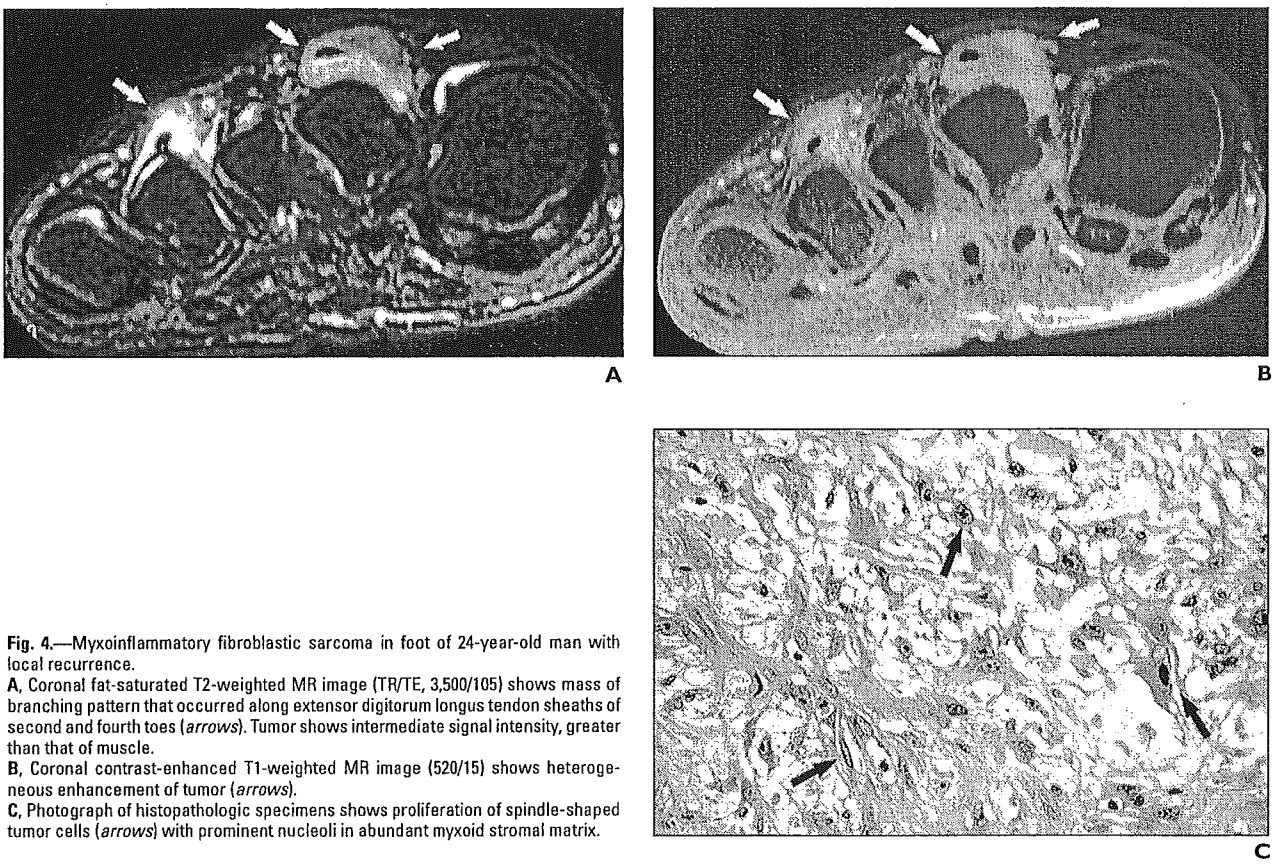

Fig. 4.—Myxoinflammatory fibroblastic sarcoma in foot of 24-year-old man with local recurrence.
A, Coronal fat-saturated T2-weighted MR image (TR/TE, 3,500/105) shows mass of branching pattern that occurred along extensor digitorum longus tendon sheaths of second and fourth toes (*arrows*). Tumor shows intermediate signal intensity, greater than that of muscle.
B, Coronal contrast-enhanced T1-weighted MR image (520/15) shows heterogeneous enhancement of tumor (*arrows*).
C, Photograph of histopathologic specimens shows proliferation of spindle-shaped tumor cells (*arrows*) with prominent nucleoli in abundant myxoid stromal matrix.

liposarcoma, and myxofibrosarcoma [9–13]. These conditions could not be distinguished radiologically from myxoinflammatory fibroblastic sarcoma on the basis of our study results. Signal characteristics and enhancement patterns were nonspecific. However, heterogeneous enhancement on contrast-enhanced MR images corresponded to geographic areas of the myxoid stromal matrix in the pathologic specimens. In two of our patients, MRI findings of recurrent tumors were ill defined and the tumors had sheetlike appearances involving the tendon sheath. A significant association may exist between recurrent tumors and the tendon sheath.

In summary, myxoinflammatory fibroblastic sarcoma typically affects adult subjects as a painless mass of the distal extremities at presentation. Myxoinflammatory fibroblastic sarcoma usually manifests on MR images as a multinodular and poorly circumscribed mass involving the surrounding tendon sheath. Although it is unlikely that such a rare condition could reasonably be diagnosed on the basis of MRI findings alone, the condition should be considered in the differential diagnosis of a soft-tissue mass in the distal extremities of adult patients.

References

1. Meis-Kindblom JM, Kindblom LG. Acral myxoinflammatory fibroblastic sarcoma: a low-grade tumor of the hands and feet. *Am J Surg Pathol* 1998;22:911–924
2. Montgomery EA, Devaney KO, Giordano TJ, Weiss SW. Inflammatory myxohyaline tumor of distal extremities with virocyte or Reed-Sternberg-like cells: a distinctive lesion with features simulating inflammatory conditions, Hodgkin's disease, and various sarcomas. *Mod Pathol* 1998;11:384–391
3. Lambert I, Debiec-Rychter M, Guelinckx P, Hagemeijer A, Sciot R. Acral myxoinflammatory fibroblastic sarcoma with unique clonal chromosomal changes. *Virchows Arch* 2001;438:509–512
4. Jurcic V, Zidar A, Montiel MD, et al. Myxoinflammatory fibroblastic sarcoma: a tumor not restricted to acral sites. *Ann Diagn Pathol* 2002;6:272–280
5. Sakaki M, Hirokawa M, Wakatsuki S, et al. Acral myxoinflammatory fibroblastic sarcoma: a report of five cases and review of the literature. *Virchows Arch* 2003;442:25–30
6. Pohar-Marinsek Z, Flezar M, Lamovec J. Acral myxoinflammatory fibroblastic sarcoma in FNAB samples: can we distinguish it from other myxoid lesions? *Cytopathology* 2003;14:73–78
7. Weiss SW, Goldblum JR. *Enzinger and Weiss's soft tissue tumors*, 4th ed. St. Louis, MO: Mosby, 2001:1552–1571
8. Mallefert JF, Dardel P, Cherasse A, Mistrih R, Krause D, Tavernier C. Magnetic resonance imaging in the assessment of synovial inflammation of the hindfoot in patients with rheumatoid arthritis and other polyarthritis. *Eur J Radiol* 2003;47:1–5
9. Llauger J, Palmer J, Monill JM, Franquet T, Bague S, Roson N. MR imaging of benign soft-tissue masses of the foot and ankle. *RadioGraphics* 1998;18:1481–1498
10. Kato K, Ehara S, Nishida J, Satoh T. Rapid involution of proliferative fasciitis. *Skeletal Radiol* 2004;33:300–302
11. Fetsch JF, Laskin WB, Miettinen M. Superficial acral fibromyxoma: a clinicopathologic and immunohistochemical analysis of 37 cases of a distinctive soft tissue tumor with a predilection for the fingers and toes. *Hum Pathol* 2001;32:704–714
12. Tateishi U, Hasegawa T, Beppu Y, Kawai A, Satake M, Moriyama N. Prognostic significance of MRI findings in patients with myxoid-round cell liposarcoma. *AJR* 2004;182:725–731
13. Munk PL, Sallomi DF, Janzen DL, et al. Malignant fibrous histiocytoma of soft tissue imaging with emphasis on MRI. *J Comput Assist Tomogr* 1998;22:819–826

World J. Surg. 29, 885–889 (2005)
DOI: 10.1007/s00268-005-7878-x

WORLD
Journal of
SURGERY

Arterial Reconstruction during Pancreatoduodenectomy in Patients with Celiac Axis Stenosis—Utility of Doppler Ultrasonography

Satoshi Nara, M.D.,[1] Yoshihiro Sakamoto, M.D.,[1] Kazuaki Shimada, M.D.,[1] Tsuyoshi Sano, M.D.,[1] Tomoo Kosuge, M.D.,[1] Yuh Takahashi, M.D.,[1] Hiroaki Onaya, M.D.,[2] Junji Yamamoto, M.D.[3]

[1]Hepatobiliary and Pancreatic Surgery Division, National Cancer Center Hospital, 5-1-1 Tsukiji, Chuo-ku, 104-0045, Tokyo, Japan
[2]Diagnostic Radiology Division, National Cancer Center Hospital, 5-1-1 Tsukiji, Chuo-ku, 104-0045, Tokyo, Japan
[3]Department of Gastrointestinal Surgery, Cancer Institute Hospital, 1-37-1 Kami-Ikebukuro, Toshima-ku, 170-8455, Tokyo, Japan

Published Online: June 16, 2005

Abstract. Celiac axis stenosis is found at an incidence of 2%–24% in the general population. During pancreatoduodenectomy in patients with celiac axis stenosis, division of the gastroduodenal artery from the common hepatic artery may cause acute ischemia of the upper abdominal organs, such as the liver, stomach, or spleen. Under these circumstances, the clinical indications of arterial reconstruction remain controversial. Between 1994 and 2003, seven patients with celiac axis stenosis (n = 4) or occlusion (n = 3) underwent pancreatoduodenectomy at our hospital. Arterial reconstruction, including division of the median arcuate ligament, was conducted in two patients; the replaced right hepatic artery was preserved in one patient, and no vascular refinement was undertaken in the remaining four of the seven patients. In two of the four patients without arterial reconstruction or preservation, the serum levels of liver enzymes were markedly elevated (> 800 IU/l) on postoperative day 1, and these patients subsequently developed liver abscesses. Two patients who underwent arterial reconstruction and three patients who showed no decrease in intrahepatic arterial flow under Doppler ultrasonography after clamping of the gastroduodenal artery developed no ischemic complications. Although our experience is limited, when intraoperative Doppler ultrasonography indicates a decrease in the hepatic arterial signals, we believe that reconstruction of the hepatic artery will be necessary to minimize ischemic complications in the liver in patients with celiac axis stenosis.

Celiac axis stenosis (CAS) is not a too rarely encountered condition. The reported incidence of CAS on angiographic examination is in the range of 12%–24% in European countries, and 2%–7% in Asian countries [1].

During pancreatoduodenectomy (PD) in patients with CAS, division of the gastroduodenal artery (GDA) from the common hepatic artery may cause abrupt ischemia of the upper abdominal organs, such as the liver, stomach, or spleen, especially if the collateral pathways from the superior mesenteric artery (SMA) are inadequate. To prevent ischemic complications in these organs, especially the liver, a variety of methods for arterial reconstruction [2–7] and preservation of the collateral pathways [8] have been reported. Some investigators argue, however, that the incidence of ischemic complications is low and that arterial reconstruction is seldom needed [9–11]. Thus, until now, the surgical indications for arterial reconstruction during PD for patients with CAS have not been established.

We review our experience of PD to assess the clinical indications for arterial reconstruction in patients with CAS, to avoid ischemic complications in the upper abdominal organs.

Patients and Methods

Patients and Diagnosis

Between 1994 and 2003, 357 patients underwent PD or pylorus-preserving PD (PPPD) at our hospital for the treatment of pancreatic cancer (n = 233), bile duct cancer (n = 55), duodenal cancer (n = 51), gallbladder cancer (n = 13), or other tumors of the pancreas head (n = 5). Whenever possible, the patients underwent preoperative angiography as part of the routine work-up. Among these, preoperative diagnosis of CA stenosis (n = 4) and occlusion (n = 3) was made in seven patients (2.0%). Celiac axis stenosis was suspected when the celiac tributaries were visualized through dilated collaterals on SMA angiography. The diagnosis of CAS was confirmed when the root of the celiac artery was stenotic on the angiographic images or in sagittal reformatted computed tomographic (CT) images. The diagnosis of celiac axis obstruction was confirmed when the root of CA could not be catheterized.

Treatments

Two patients underwent arterial revascularization. In one patient, division of the median arcuate ligament (MAL) was carried out (case 1, Table 1). The other patient in whom marked decrease of the intrahepatic arterial flow was visualized on Doppler ultrasonography (US) after the division of GDA, anastomosis between the middle colic artery (MCA) and the right gastroepiploic artery (RGEA) was performed (case 2). In another patient, the replaced right hepatic artery was preserved to maintain arterial flow into

Correspondence to: Yoshihiro Sakamoto, M.D., e-mail: yosakamo@ncc.go.jp

Table 1.

Case no.	Patient	Disease	CA status	Etiology	Adopted procedure	Doppler Us		GOT/GPT (1POD) (IU/l)	Ischemic complications	Discharge (POD)
						GDA clamp	After reconstruction			
1	65M	Ph Ca	Stenosis	MAL compression	Cutting of MAL	↓	↑	119/117	None	31
2	57M	Duo Ca	Occlusion	Atherosclerosis	MCA-RGEA anastomosis	↓	↑	1166/1221	None	35
3	61F	Duo Ca	Occlusion	Atherosclerosis	Preservation of replaced RHA	→	—	73/87	None	128
4	64F	Ph Ca	Stenosis	Unknown	None	↑	—	118/95	None	31
5	86M	Ph Ca	Stenosis	Unknown	None	↑	—	121/131	None	52
6	48M	Ph Ca	Occlusion	CHA injury during angiography	None	↓	—	1396/1261	Liver abscess (POD 30)	60
7	55M	Ph Ca	Stenosis	Unknown	None	Not done	—	867/1019	Liver abscess (POD 52)	126

CA: celiac axis; GOT: glutamic oxaloacetic transaminase; GPT: glumatic pyruvic transaminase; Ph Ca: pancreatic head cancer; Duo Ca: duodenal cancer; MAL: median arcuate ligament; MCA: middle colic artery; RGEA: right gastroepiploic artery; CHA: common hepatic artery; RHA: right hepatic artery; POD: postoperative day; ↓: decrease of the intrahepatoc arterial flow; →: no remarkable change; ↑: increase of the intrahepatic arterial flow; US: ultrasound

the liver (case 3). The remaining four patients did not undergo any arterial reconstruction or preservation, based on the respective surgeons judgment.

Results

There was no postoperative mortality. In two out of the four patients (Cases 6 and 7) who did not undergo arterial reconstruction or preservation, the serum levels of the hepatic transaminases became markedly elevated (> 800 IU/L) on postoperative day 1, and these patients subsequently developed liver abscesses on postoperative days 30 and 52, respectively. The two patients (cases 1 and 2) who underwent arterial reconstruction and three patients (cases 3–5) who showed no decrease of intrahepatic arterial flow in on Doppler US after clamping of the GDA did not develop any ischemic complications. One patient (case 3) in whom the replaced right hepatic artery was preserved developed leakage of the pancreatojejunostomy, which was not attributed to ischemia (Table 1).

Case 1

A 65-year-old man presented with obstructive jaundice. Contrast-enhanced abdominal CT revealed a low-attenuation mass, 20 × 15 mm in size, located in the pancreatic head. On SMA angiography, the hepatic and splenic arteries were visualized serially via the GDA (Fig. 1A). Severe stenosis of the celiac artery at its root was demonstrated on sagittal reformatted CT imaging (Fig. 1B), and the CT image showed that some fibrous tissue connecting with bilateral curs covered the supraceliac aorta. Thus, a diagnosis of pancreatic cancer with CAS caused by compression of the MAL was made. The proposed operation was PPPD with possible arterial reconstruction.

After occlusion of the GDA, intraoperative Doppler US revealed an apparent decrease in the intrahepatic arterial flow (Fig. 2B), and thick fibrous tissue (MAL) was found to be masking the CA (Fig. 2A). The MAL was divided longitudinally and the root of the CA was fully exposed (Fig. 3 A). After division of the MAL, a marked increase in the intrahepatic arterial signals was observed, even with clamping of the GDA (Fig. 3B). Thereafter, the GDA was ligated and divided and PPPD was performed in the usual manner. The patient's postoperative course was uneventful and he was discharged on postoperative day 31.

Discussion

The surgical indications for hepatic arterial reconstruction during PD in patients with CAS remain unclear. Two of the four patients (50%) in our experience who did not undergo arterial reconstruction or preservation developed liver abscesses, whereas none of the three who underwent arterial reconstruction or preservation developed any ischemic complications. Even though our experience is limited, these results indicate that some form of arterial reconstruction may be necessary to avoid or minimize ischemic complications, when intraoperative Doppler US reveals a decrease in intrahepatic arterial signals. The preservation of collateral pathways from SMA to CA tributaries may be preferred, provided the collaterals are free from tumor invasion.

In the series reported until now, division of the GDA during PD in patients with CAS did not always result in ischemic

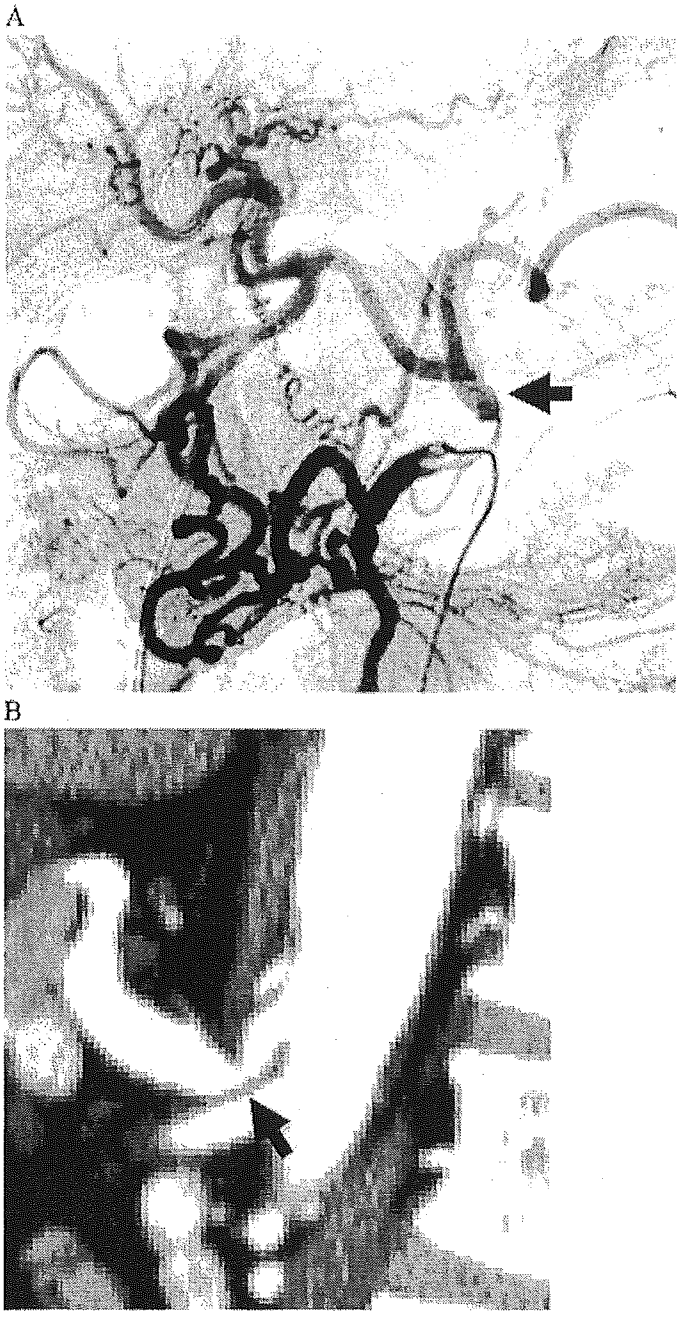

Fig. 1. A. On superior mesenteric arteriography, the common hepatic artery and splenic artery were visualized serially via the gastroduodenal artery. The arrow shows the root of the celiac axis. B. Sagittal reformatted CT image reveals severe stenosis (arrow) of the celiac axis.

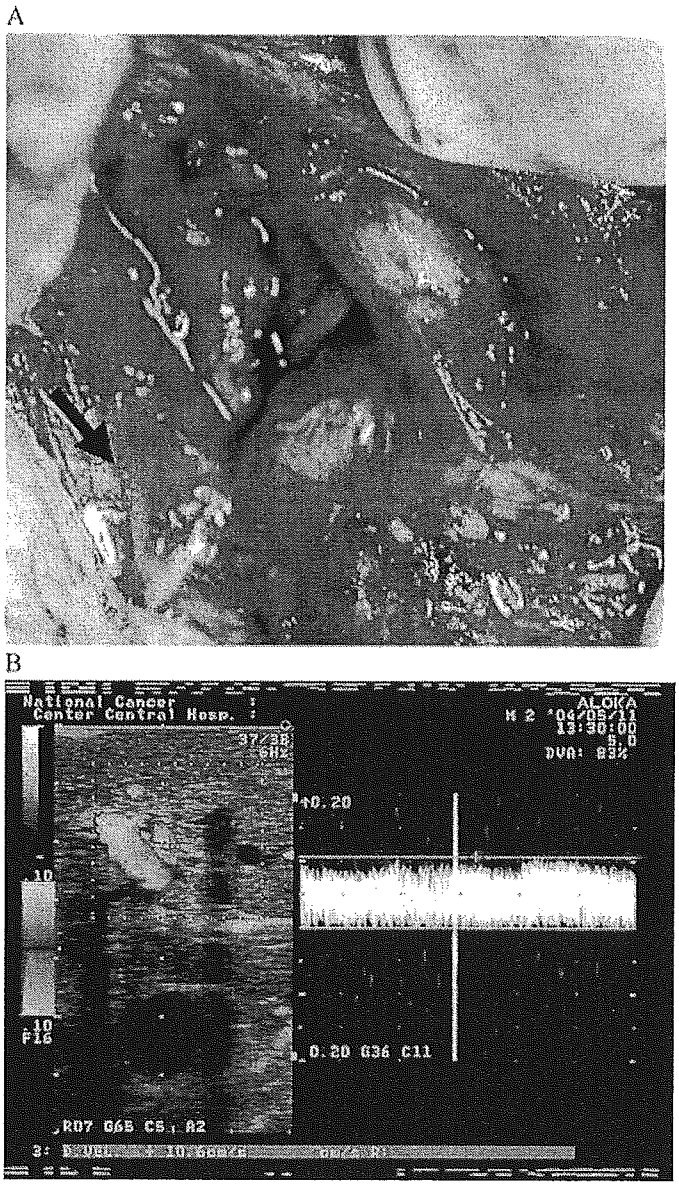

Fig. 2. A. The median arcuate ligament (arrow) masking the root of the celiac axis. B. After clamping of the gastroduodenal artery, intraoperative Doppler ultrasonography revealed an apparent decrease in the intrahepatic arterial flow.

complications of the upper abdominal organs. Both Trede [9] and Berney et al. [10] reported that only 13%–17% of patients with CAS required arterial reconstruction during PD attributed to the abundant collateral anastomosis between the CA tributaries and SMA tributaries other than the pancreatic head arcade. Among 94 Korean patients with CAS, collateral pathways, such as from the dorsal pancreatic artery or replaced right hepatic artery, existed in about 80% of the patients [12]. With these collaterals, hepatic arterial flow can be maintained even after division of the GDA, as in our case 3. However, in patients with malignant tumors, preservation of these collaterals during PD is often impossible, or it may be undesirable on account of the need to ensure surgical curability, and arterial restoration may become imperative.

We believe that intraoperative Doppler US is highly useful for informing the decision for or against arterial reconstruction, as shown in cases 1 and 2. The usefulness of intraoperative Doppler US has been demonstrated during liver transplantation [13], and this practical and convenient modality has now become indispensable for the confirmation of arterial flow during hepatobiliary-pancreatic surgery. We propose that a final decision on arterial reconstruction before the division of GDA be made using intraoperative Doppler US.

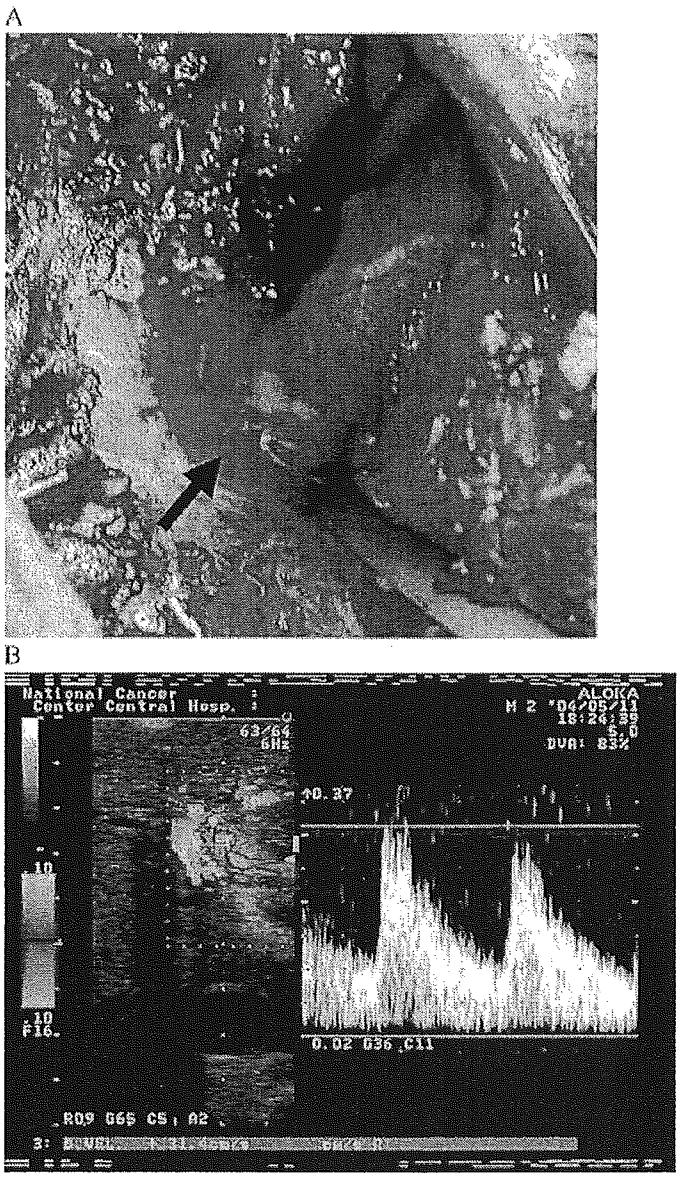

Fig. 3. A. The root of celiac axis (arrow) is exposed. **B.** Doppler ultrasonography shows a dramatic increase in the intrahepatic arterial signal.

The etiology of CAS can be divided into three categories;(1) extrinsic stenosis from compression by the MAL or the celiac ganglion. (2) intrinsic stenosis from atherosclerosis, (3) other causes, including congenital causes, tumor invasion, compression by a swollen pancreas in cases of pancreatitis, or injury during angiography [10, 14]. In a Korean report, among 400 consecutive angiographic examinations in patients with liver tumors, 7:3% showed CAS, and the etiology was determined to be extrinsic compression in 55% of patients, intrinsic stenosis in 10%, and other causes, in 35% [14]. In contrast, in Western studies, the most frequent etiology was atherosclerosis [10].

Revascularization procedures must be chosen according to the etiology of CAS. When CA stenosis is caused by extrinsic compression, division of the MAL or the fibrous celiac ganglion is a simple and effective method, as in case 1. Preoperative stenting of

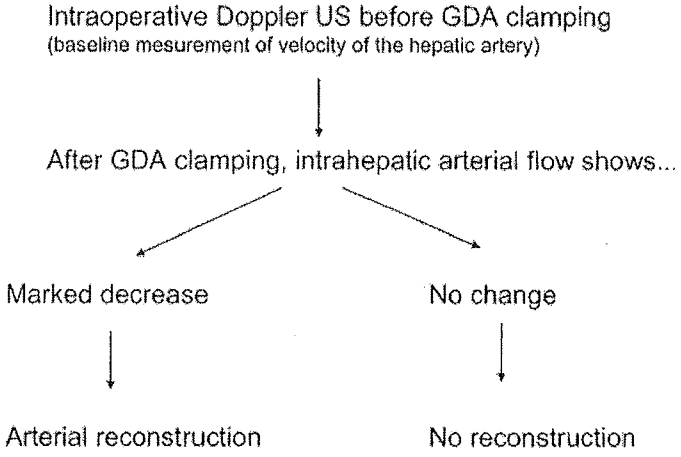

Fig. 4. Recommended steps for the decision on arterial reconstruction.

the CA, although reported to be successful in one reported case [15], was avoided by us, because of the risk of stent-crushing due to persistent external compression, as described by Sharafuddin et al. [16]. For patients with an atherosclerotic etiology, there are many reports of successful endovascular treatments [16, 17]. While the immediate success rate has been reported to be 81%–96%, the long-term success rate still remains unknown.

As for surgical reconstruction, a variety of methods have been reported, such as bypass between the aorta and the CA [4], between the splenic artery and the SMA [5], or between the aorta and the common hepatic artery, occasionally using a venous graft [2, 3]. Machado et al. reported successful reconstruction by means of anastomosis of the MCA to the GDA stump [6]. Okamoto et al. advocate a venous graft bypass between the iliac artery and the splenic artery, because the vascular anastomosis is away from the pancreatojejunostomy and the risk of exposure to pancreatic juice is minimal [7]. Thus, there is no single best procedure, and the method of arterial reconstruction used must be selected according to the surgical condition of the individual patient.

In our series, all three patients (Cases 3–5) who showed no decrease of hepatic inflow after GDA clamping developed no ischemic complication, possibly because there were enough hepatopetal collateral arteries. We therefore suppose that sustained hepatic flow after the GDA clamping indicates no need for arterial reconstruction if collaterals can be preserved. Nevertheless we believe that any patient who demonstrates a decrease in hepatic arterial flow after GDA clamping has the possibility of suffering from ischemic complications. We recommend arterial reconstruction when a moderate or severe decrease in hepatic arterial inflow is observed with Doppler US (Fig. 4). But this is a small number of patients. To establish definitive criteria for hepatic arterial reconstruction during PD for patients with CAS, a large number of patients should be studied based on the precise evaluation of the velocity of hepatic arterial inflow using Doppler US.

In conclusion, we performed PD in seven patients with CAS and encountered ischemic complications in two who underwent no arterial reconstruction. Another two patients underwent arterial reconstruction based because we observed a decrease in intrahepatic arterial flow, and neither of them developed ischemic complications. Three other patients who showed no decrease intrahepatic arterial flow on Doppler US after clamping of the GDA had an uncomplicated postopuative course. We therefore

consider that hepatic arterial reconstruction is necessary during PD in patients with CAS when intraoperative Doppler US shows a significant decrease in intrahepatic arterial signal after clamping of the GDA.

References

1. Kwon JW, Chung JW, Song SY, et al. Transcatheter arterial chemoembolization for hepatocellular carcinomas in patients with celiac axis occlusion. J. Vase. Interv. Radiol. 2002;13:689–694
2. Miyata M, Takao T, Okuda A, et al. Pancreatoduodenectomy for periampullary cancer associated with celiac occlusion: a case report. Surgery 1988;103:261–263
3. Manabe T, Baba N, Setoyama H, et al. Venous bypass grafting for celiac occlusion in radical pancreaticoduodenectomy. Pancreas 1991; 6:368–371
4. Takach TJ, Levesay JJ, Reul GJ Jr., et al. Celiac compression syndrome: tailored therapy based on intraoperative findings J. Am. Coll. Surg. 1996;183:606–610
5. Thompson NW, Eckhauser FE, Talpos G, et al. Pancreaticoduodenectomy and celiac occlusive disease. Ann. Surg. 1981;193:399–406
6. Machado MC, Penteado S, Montagnini AL, et al. An alternative technique in the treatment of celiac axis stenosis diagnosed during pancreaticoduodenectomy. HPB Surg. 1998;10:371–373
7. Okamoto H, Suminaga Y, Toyama N, et al. Autogenous vein graft from iliac artery to splenic artery for celiac occlusion in pancreaticoduodenectomy. J. Hepatobiliary Pancreat. Surg. 2003;10:109–112
8. Kurosaki I, Hatakeyama K, Nihei KE, et al. Celiac axis stenosis in pancreaticoduodenectomy. J. Hepatobiliary Pancreat. Surg. 2004; 11:119–124
9. Trede M. The surgical treatment of pancreatic carcinoma. Surgery 1985;97:28–35
10. Berney T, Pretre R, Chassot G, et al. The role of revascularization in celiac occlusion and pancreatoduodenectomy. Am. J. Surg. 1998; 176:352–356
11. Pfeiffenberger J, Adam U, Drognitz O, et al. Celiac axis stenosis in pancreatic head resection for chronic pancreatitis. Langenbecks Arch. Surg. 2002;387:210–215
12. Song SY, Chung JW, Kwon JW, et al. Collateral pathways in patients with celiac axis stenosis: angiographic-spiral CT correlation. Radiographics 2002;22:881–893
13. Sakamoto Y, Harihara Y, Nakatsuka T, et al. Rescue of liver grafts from hepatic artery occlusion in living-related liver transplantation. Br. J. Surg. 1999;86:886–889
14. Park CM, Chung JW, Kim HB, et al. Celiac axis stenosis: incidence and etiologies in asymptomatic individuals. Korean J. Radiol. 2001;2:8–13
15. Hasegawa K, Imamura H, Akahane M, et al. Endovascular stenting for celiac axis stenosis before pancreaticoduodenectomy. Surgery 2003;133:440–442
16. Sharafuddin MJ, Olson CH, Sun S, et al. Endovascular treatment of celiac and mesenteric arteries stenoses: applications and results. J. Vasc. Surg. 2003;38:692–698
17. van Wanroij JL, van Petersen AS, Huisman AB, et al. Endovascular treatment of chronic splanchnic syndrome. Eur. J. Vasc. Endovasc. Surg. 2004;28:193–200

Preparation and Biological Characterization of Polymeric Micelle Drug Carriers with Intracellular pH-Triggered Drug Release Property: Tumor Permeability, Controlled Subcellular Drug Distribution, and Enhanced in Vivo Antitumor Efficacy

Younsoo Bae, Nobuhiro Nishiyama, Shigeto Fukushima, Hiroyuki Koyama, Matsumura Yasuhiro, and Kazunori Kataoka

Department of Materials Science and Engineering, Graduate School of Engineering, The University of Tokyo, 7-3-1 Hongo, Bunkyo-ku, Tokyo 113-8656, Japan, Department of Clinical Vascular Regeneration, Graduate School of Medicine, The University of Tokyo, 7-3-1 Hongo, Bunkyo-ku, Tokyo 113-8655, Japan, and Investigative Treatment Division, National Cancer Center Research Institute East, 6-5-1 Kashiwanoha, Kashiwa, Chiba 277-8577, Japan

Bioconjugate Chemistry®

Reprinted from
Volume 16, Number 1, Pages 122–130

Preparation and Biological Characterization of Polymeric Micelle Drug Carriers with Intracellular pH-Triggered Drug Release Property: Tumor Permeability, Controlled Subcellular Drug Distribution, and Enhanced in Vivo Antitumor Efficacy

Younsoo Bae,[†] Nobuhiro Nishiyama,[‡] Shigeto Fukushima,[†] Hiroyuki Koyama,[‡] Matsumura Yasuhiro,[§] and Kazunori Kataoka*,[†]

Department of Materials Science and Engineering, Graduate School of Engineering, The University of Tokyo, 7-3-1 Hongo, Bunkyo-ku, Tokyo 113-8656, Japan, Department of Clinical Vascular Regeneration, Graduate School of Medicine, The University of Tokyo, 7-3-1 Hongo, Bunkyo-ku, Tokyo 113-8655, Japan, and Investigative Treatment Division, National Cancer Center Research Institute East, 6-5-1 Kashiwanoha, Kashiwa, Chiba 277-8577, Japan. Received July 28, 2004; Revised Manuscript Received October 31, 2004

A novel intracellular pH-sensitive polymeric micelle drug carrier that controls the systemic, local, and subcellular distributions of pharmacologically active drugs has been developed in this study. The micelles were prepared from self-assembling amphiphilic block copolymers, poly(ethylene glycol)-poly(aspartate hydrazone adriamycin), in which the anticancer drug, adriamycin, was conjugated to the hydrophobic segments through acid-sensitive hydrazone linkers. By this polymer design, the micelles can stably preserve drugs under physiological conditions (pH 7.4) and selectively release them by sensing the intracellular pH decrease in endosomes and lysosomes (pH 5–6). In vitro and in vivo studies show that the micelles have the characteristic properties, such as an intracellular pH-triggered drug release capability, tumor-infiltrating permeability, and effective antitumor activity with extremely low toxicity. The acquired experimental data clearly elucidate that the optimization of both the functional and structural features of polymeric micelles provides a promising formulation not only for the development of intracellular environment-sensitive supramolecular devices for cancer therapeutic applications but also for the future treatment of intractable cancers with limited vasculature.

INTRODUCTION

The selective augmentation of drug concentrations in avascular tumor tissues is the most challenging issue of current cancer chemotherapy using macromolecular bioconjugates (*1–3*). Most anticancer drugs are pharmacologically effective but limited in their clinical applications due to serious toxicity and low water solubility; thereby, the altered biodistribution of these drugs has an important meaning not only to reduce the toxicity but also to improve therapeutic effects (*4–6*). For these reasons, interest has centered on the creation of drug carriers that safely and precisely deliver the appropriate amounts of active drugs to solid tumors (*7–10*). Indeed, several macromolecular drug carriers are under clinical trials or used practically, which include water-soluble polymer–drug conjugates (*11*), liposomal carriers (*12*), and polymeric micelles (*13*). However, even though these carriers have made significant advancements in cancer therapy, recent studies point out their antitumor activities are subject to change according to the cancer species with pathological, pharmacological, and biochemical differences (*14*).

* To whom correspondence should be addressed. Phone: +81-3-5841-7138, Fax: +81-3-5841-7139, E-mail: kataoka@bmw.t.u-tokyo.ac.jp.

† Department of Materials Science and Engineering, The University of Tokyo.

‡ Department of Clinical Vascular Regeneration, The University of Tokyo.

§ National Cancer Center Research Institute East.

There are three major reasons why the present macromolecular drug carriers have difficulties in clinical use. First, the carriers injected into the body encounter in vivo barriers such as nonspecific systemic accumulation and phagocytotic clearance by the host defense system (*15*). Second, even after the carriers accumulated in solid tumors avoiding these in vivo barriers, they still have to overcome the heterogeneous tumor microenvironments that are characterized by insufficient blood supply, disordered vasculatures, and diffusion-limited interstitum (*16*). Third, the carriers that successfully accessed the inside of tumor tissues should release the loaded drugs back into active forms in order to exert the antitumor effect (*17*). Among these reasons, poor permeability of the carriers inside the tumor tissues and low concentrations of active drugs throughout solid tumors become particularly serious problems (*18, 19*). For these reasons, understanding the correlation between the physicochemical properties of drug carriers and their behaviors in the body is very important, and the combination of these two features is required for the design of ultimate carriers (*20*).

In this article, we will report that such tantalizing problems may be overcome by a novel tumor-infiltrating drug carrier, the pH-sensitive polymeric micelle, whose structural and functional features were optimized for the intracellular drug delivery (Figure 1A). The micelle is a nanosized supramolecular assembly from the self-assembling amphiphilic block copolymers, poly(ethylene glycol)-poly(aspartate hydrazone adriamycin) [PEG-p(Asp-Hyd-ADR)]. The anticancer drug, adriamycin (ADR), is

10.1021/bc0498166 CCC: $30.25
Published on Web 12/22/2004

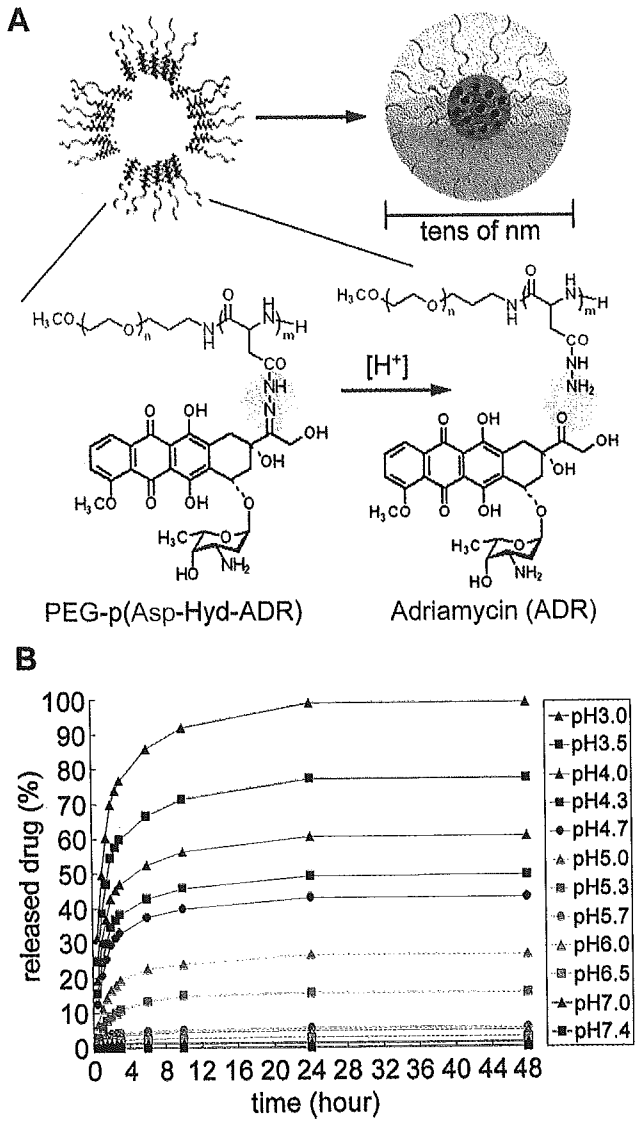

Figure 1. Preparation of tumor-infiltrating polymeric micelles with intracellular pH-sensitivity. (A) Micelles with tens of nm size diameter were prepared from self-assembling amphiphilic block copolymers, PEG-p(Asp-Hyd-ADR), in which the anticancer drug, adriamycin (ADR), was conjugated through acid-sensitive hydrazone linkers. (B) The micelles released the loaded drugs under acidic conditions below pH 6.0 corresponding to intracellular space, but remained stable under the conditions of vascular and extracellular space (pH 7.4–7.0).

conjugated to the core-forming segments through the hydrazone linkers that are stable under physiological conditions (pH 7.4) but cleavable under acidic intracellular environments in endosomes and lysosomes (pH 5–6). This carrier design allows the micelle to safely protect hydrophobic drugs from the host defense system in the body and to selectively exert cytotoxicity due to intracellular pH-triggered drug release, improving both the delivery effect and therapeutic efficacy of the drugs (*21*). Therefore, the characteristic in vitro and in vivo behaviors of the micelles would offer intriguing information taking into account the future design and development of bioresponsive supramolecular carrier systems for the intracellular trafficking of biologically active molecules.

EXPERIMENTAL PROCEDURES

Materials. β-Benzyl-L-aspartate was from Sigma and α-methoxy-ω-amino poly(ethylene glycol) (PEG; MW = 12 000) was from Nippon Oil & Fats, Japan. PEG was purified using an ion-exchange gel column (CM-Sephadex C-50, Amersham Pharmacia Biotech) prior to the synthesis of the block copolymers. Adriamycin hydrochloride-(ADR–HCl) was from Nippon Kayaku, Japan, and its purity was checked by reversed phase liquid chromatograpy (RPLC). Sephadex LH-20 gel was from Amersham Pharmacia Biotech, Sweden.

Cell Lines and Animals. A human small cell lung cancer cell line SBC-3 and murine colon adenocarcinoma 26 (C26) cells were from the National Cancer Center Research Institute, Japan, and cultured in a medium (DMEM, Sigma, St. Louis, MO) containing 10% fetal bovine serum in a humidified atmosphere with 5% CO_2 at 37 °C. CDF-1 mice (female, 6 weeks old) were from Charles River, Japan. The animals were cared for and all experiments were performed in compliance with the Guide for the Care and Use of Laboratory Animals as adopted and promulgated by the National Institutes of Health.

Preparation of the pH-Sensitive Polymeric Micelles. The self-assembling amphiphilic block copolymer, PEG-p(Asp-Hyd-ADR), was synthesized as reported elsewhere (*22*). Briefly, poly(ethylene glycol)-poly(β-benzyl-L-aspartate) (PEG-PBLA) was synthesized from the ring-opening polymerization of β-benzyl-L-aspartate *N*-carboxyanhydride using PEG as a macro initiator, followed by substitution of the benzyl groups of PEG-PBLA with hydrazide groups for drug binding (see also Supporting Information). Unbound ADR was completely removed using Sephadex LH-20 gel, and the obtained polymers were redissolved in dimethylacetamide to prepare the micelle by a dialysis method.

Evaluation of Acid-Sensitive Drug Release from the Micelles. Reversed phase liquid chromatograpy (RPLC) analysis, using a μ-Bondasphere 5 μm C4-300A column (Nihon Waters, Japan), was used to assess the pH sensitivity of the micelle. The micelle with a 10 mg/mL concentration was incubated under various buffered conditions from pH 7.4 to 3.0 [20 mM phosphate buffer (pH 7.4–6.0), 20 mM acetate buffer (pH 5.8–3.0)], and time- and pH-dependently released drugs were measured from the peak intensity by a UV detector (485 nm).

Observations on Intracellular Drug Release and Localization of the Micelles. Multicellular tumor spheroid (MCTS) was prepared from a C26 cell line using a spheroid culture plate, Sumiloncelltight (Sumitomo Bakelite, Japan); 200 μm size MCTS were sorted and used for the experiments. Fluorescence images were observed using a confocal laser scanning microscope (LSM 510, Carl Zeiss, Germany) with a 20× objective (Plan-Apochromat, Carl Zeiss, Germany) and a 63× objective (C-Apochromat, Carl Zeiss, Germany) at excitation wavelengths of 488 nm (Ar laser) and 364 nm (UV laser) for ADR and Hoechst 33258, respectively. The concentrations of the micelles in the medium were adjusted to 10 μg/mL (ADR equivalent). All images were acquired and processed with the accompanying software.

In Vitro Growth Inhibition Assay. A tetrazolium dye method, called the MTT assay, was used to evaluate the growth-inhibitory effect of the micelle. Using 96-well culture plates, exponentially growing SBC-3 cells were seeded (2000 cell/well) and preincubated for 24 h, followed by coincubation with ADR and the micelle samples. After exposure for 3, 10, and 24 h, the medium was discarded and each cell was reincubated in fresh medium for another 24 h. The cells were then counted using a Bio-RAD Microplate Reader 550 (Bio-Rad Laboratories Inc.).

In Vivo Antitumor Activity and Body Weight Change of Mice. The antitumor activity of the micelles was evaluated with tumor bearing, 7-week-old, female SPF CDF1 mice (n = 6, Charles River, Japan). After implanting C26 cells 10 days earlier, injection of the samples took place using a volume of 0.1 mL/10 g body weight. The regimens of the micelles were scheduled by changing the administration dose (20, 40, and 60 mg/kg) three times with a 4-day interval, based on the optimized regimens of ADR as a control. However, in the case of ADR, only limited doses (5, 10, and 15 mg/kg) were applied to the mice due to the drugs toxicity. The mice were monitored daily, and tumor growth and body weights were measured at 2-day intervals. Tumor volume is calculated as follows: volume = $1/2 \times LW^2$ (L is the long diameter and W is the short diameter of a tumor).

Biodistribution and Pharmacokinetics. The CDF1 mice (n = 6), when the tumor volume reached ca. 100 mm^3, were injected with ADR and the micelles in a volume of 0.1 mL/10 g body weight for the experiments. The dose was either 10 mg/kg for ADR or the micelles (ADR equivalent). After the injection, blood, tumor, and major organs (heart, kidney, liver and spleen) were collected at 0.5, 1, 3, 6, 9, 24, and 48 h, followed by HPLC anaylsis (see Supporting Information for the detailed protocol).

Fluorescence Microscopic Observations of Solid Tumors and Their Peripheral Blood Vessels. The tumor-bearing mice were sacrificed at 24 h after the injection of the micelles with a 10 mg/kg dose. The intact tumor tissues with their peripheral blood vessels were harvested for macroscopic observations using a fluorescence microscope (Axiovert 200, Carl Zeiss, Germany) equipped with a 2.5× objective (Plan-Neofluar, Carl Zeiss, Germany) and a filter set15 (BP546/12, FT580, LP590, mercury lamp excitation, Carl Zeiss, Germany).

RESULTS

Preparation of the Intracellular pH-Sensitive Polymeric Micelles. The polymer backbone of PEG-p(Asp-Hyd-ADR) consisted of poly(ethylene glycol) (PEG) with a molecular weight of 12 000 g/mol for the hydrophilic shell-forming segment and 37 repeating units of polyaspartate (PAsp) for the core-forming segment (MW = 28 679), which were determined by gel permeation chromatography and ^{1}H NMR measurements. The 28 side chains in the PAsp block were replaced by hydrazide groups for the binding of the drugs. Adriamycin (ADR) was then conjugated to the polymer backbone through hydrazone bonds between the carbonyls at the C13 of ADR and the hydrazide groups of the PEG-p(Asp-Hyd) block copolymer. Even though the biological and chemical background of binding ADR to polymer backbone through hydrazone linkages has been delineated in our previous work (*22*) as well as many studies (*23*–*26*), it must be noticed that the hydrazone linkage is the most popularly used as pH-sensitive linkers due to the fact that this bond is quite stable at pH 7.4 but hydrolyzes under mild acidic conditions with pH 5–6. Therefore, to ensure that drug release from the micelles occurs only when acid-labile hydrazone linkers are cleaved, any unbound free ADR were completely removed in this study. These were confirmed by a reversed phase liquid chromatograpy (RPLC) analysis that is generally used for separating and purifying materials due to the differences in their hydrophobic properties (further details are described below). RPLC analysis showed the drug loading content of PEG-p(Asp-Hyd-ADR) was 42.5 wt % with respect to a single block copolymer chain. The obtained PEG-p(Asp-Hyd-ADR) block copolymers self-assembled into micelles in aqueous solutions; the prepared micelles had a 65 nm diameter, which was confirmed by dynamic light scattering measurements.

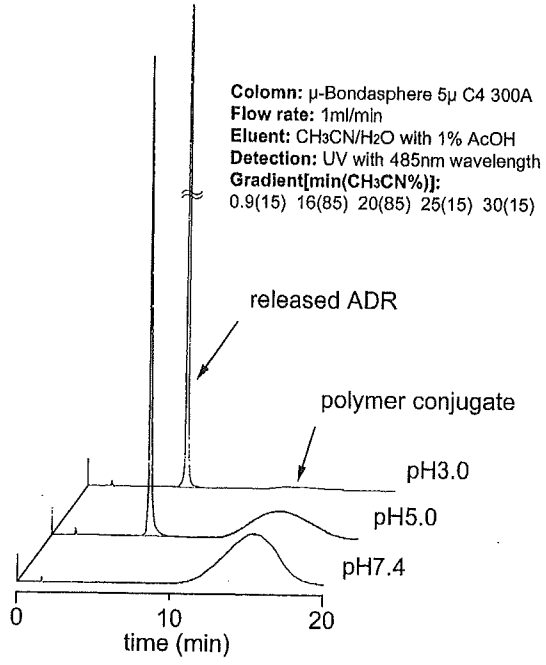

Figure 2. Acid-sensitive cleavage of drug-binding hydrazone bonds evaluated by reversed phase liquid chromatography (RPLC) analysis. RPLC separates free drugs and polymer conjugates due to the differences in their hydrophobic properties, demonstrating absence of free drugs at pH 7.4 possibly binding to polymer conjugates in a physical way. On the other hand, it clearly shows that the amount of released drugs increases under acidic conditions in which the drug-binding hydrazone linkers can be cleaved.

The Micelles Selectively Release the Loaded Drugs by Sensing a pH Decrease. To confirm the acid-sensitive drug release profile, the micelles were incubated under various pH conditions from 7.4 to 3.0, and the released drugs were measured using RPLC analysis. Figure 1B shows that the micelles released the loaded drugs time- and pH-dependently as the external pH decreased, while they were stable under physiological conditions at pH 7.4 for over 48 h. The results indicate the micelles should release the loaded drugs in the intracellular acidic regions (pH 5–6) such as endosomes and lysosomes in which the drug-binding hydrazone linkers can be cleaved most effectively. Chemical evidence for absence of free drugs and acid-sensitive cleavage of hydrazone linkers to induce drug release was also presented by RPLC analysis (Figure 2). As described above, ADR is conjugated to amphiphilic block copolymers through pH-sensitive hydrazone linkers. If the drugs were simply entrapped in the micelles by physical interaction instead binding to polymers via chemical linkers, a sharp peak corresponding to the free drug should be separated from drug–polymer conjugates by RPLC and appeared in the physiological condition (pH 7.4) where the acid-labile hydrazone bond remains stable. However, the peak from the free drug was not shown at pH 7.4 but gradually increased in acidic conditions while the broad peak from polymer conjugates decreased. Eventually, almost 100% of the drugs were released at pH 3.0, and on the basis of this, we calculated the drug loading content of polymer conjugate described above. These results demonstrate that acid-sensitive cleavage

Table 1. Growth Inhibitory Effects of the Micelles against Cancer Cells[a]

sample	exposure time (hour)	IC_{50}[b] (μg/mL±SD)	relative index[c]
ADR	3	0.041 ± 0.035	1.05
	10	0.048 ± 0.026	1.23
	24	0.039 ± 0.025	1
micelle	3	1.08 ± 0.12	27.69
	10	0.45 ± 0.061	11.54
	24	0.27 ± 0.038	6.92

[a] Eight independent experiments were carried out using a human small cell lung cancer cell line SBC-3 ($n = 8$). [b] IC_{50} denotes the inhibitory concentration of the drugs required for 50% reduction in cell population. Concentrations of the micelles are calculated with free ADR equivalents. [c] Relative index denotes the ratio between a control and the object for comparison. Here, we evaluated the growth inhibitory effect of the micelles by converting their concentrations with respect to ADR after a 24 h incubation as the control.

of hydrazone linkers between drugs and polymer chains obviously induced drug release.

Regenerated Drugs Were Pharmaceutically Active Inhibiting Cell Growth in Vitro. To verify whether the released drugs are pharmacologically active, an in vitro growth-inhibition test was carried out. The test revealed that the cytotoxic activity of the micelles was as high as 1/7-fold with respect to that of the free drugs after a 24 h exposure time (Table 1). Interestingly, the micelles showed delayed cytotoxicity that was drastically changed depending on the incubation time, which reflects that the drug release from the micelles took place and correlated with the cell metabolism.

The Micelle Infiltrates into the Avascular Tumor Model Multicellular Tumor Spheroids. Recently, it has been reported that the fluorescence quenching effect of the micelles provides a useful tool to observe the intracellular behaviors of the micelles (*22*). The fluorescence intensity of ADR, playing a role not only as an anticancer drug, but also as a fluorescence probe in this study, is quenched due to the locally increased high concentration in the micelle core; however, the fluorescence becomes detectable again as the micelles start to release ADR under acidic conditions. Consequently, the micelles emit intense fluorescence signals with the release of the entrapped ADR; a series of processes such as intracellular trafficking, drug release, and localization were able to be directly monitored in live cells accompanying the structural change. In the meantime, the multicellular tumor spheroid (MCTS) was used as an in vitro tumor model for the experiments because it is the most similar to avascular tumor regions of practical solid tumors in vivo that are characterized by limited accessibility of cell subpopulations (Figure 3). For example, MCTS reproduces adverse microenvironmental conditions of solid tumors in vivo such as hypoxia and nutritional depletion, and the extracellular matrix between tumor cells instead of intratumoral normal cell populations (*27*–*28*).

For these reasons, the intracellular behaviors of the micelles were observed within solid tumors using fluorescence quenching effect and the MCTS. The micelles were coincubated with the MCTS, and the change in the fluorescence intensity was monitored using a confocal laser scanning microscope (CLSM). The three-dimensional CLSM images demonstrated the time-dependent change in the fluorescence intensity of the micelle systems and their distributions throughout the MCTS with a 200 μm diameter depending on the incubation time (Figure 4A). The 200 μm diameter of MCTS was

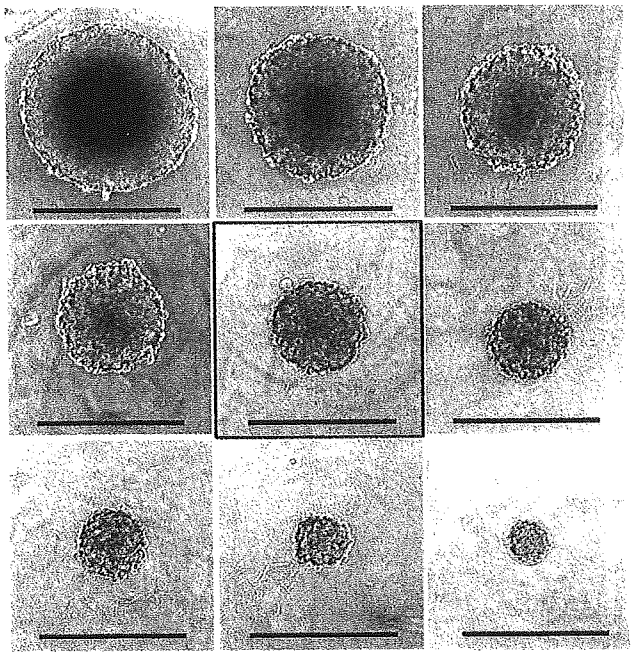

Figure 3. Preparation of multicellular tumor spheroid (MCTS). MCTS with diameter ranging from 100 to 500 μm was prepared from a C26 cell line. Among them, MCTS with a 200 μm diameter (red-edged) was used as an in vitro tumor model because it has the most suitable size for reproducing in vivo avascular tumor regions that are characterized by limited accessibility of cell subpopulations (bar = 500 μm).

determined as the most suitable size for the experiments, considering the fact that the maximum distance between the capillary blood vessels within avascular solid tumor is 200 μm or less (*29*). The fluorescence of the micelle system remained quenched at 1 h after incubation, but it was detected at 3 and 24 h. It is notable that most cell nuclei remained blue at 3 h. The images, therefore, suggest that the micelles began to intracellularly release the drugs but the released drugs were still localized in the cytoplasm. However, the intense fluorescence of ADR was eventually detected in most of the cell nuclei after 24 h. These results reflect that the micelles would access every cell in the avascular region of tumor tissues in vivo to release the drugs.

The Micelles Enter the Cell Interior and Release the Drugs. To get a better understanding of the intracellular distributions of the micelles and their released drugs, further observations of the MCTS coincubated with the micelles under high magnification were carried out using a 63× objective (Figure 4B). These images show clear evidence of the intracellular drug release from the micelles and accumulation of the released drugs in the cell nuclei. The localization of the ADR fluorescence in the cytoplasm after 3 h incubation is supporting our speculation that the micelles internalized the cells releasing the drugs. After additional incubation up to 24 h, the presence of the drugs both in the cytoplasm and cell nuclei was confirmed. When the same experiments were carried out with free ADR, all the cell nuclei in the MCTS became red within 1 h because the ADR with a low molecular weight rapidly penetrated into each cell, and we were not able to observe this unique time-dependent fluorescence change in intensity and its distribution. Therefore, it is obvious that the micelles are precisely functioning in the intracellular regions as we designed, and the possible drug release from the micelles in the extracellular regions is negligible.

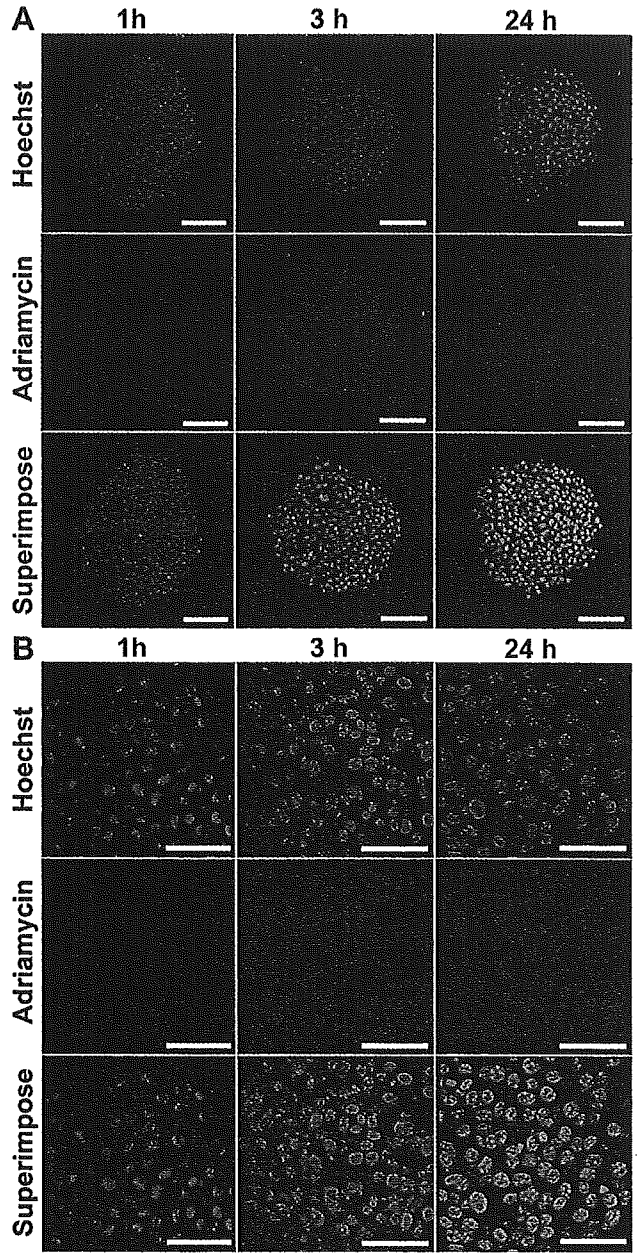

Figure 4. Observation of tumor permeability and intracellular drug release behaviors of the micelles. (A) CLSM observations showed the time-dependent change in the fluorescence intensities of ADR in the micelle system in MCTS. The images showed that the micelles can access the inside of the MCTS and release the loaded drugs (bar = 100 μm). (B) The intracellular drug release and localization of the micelles in each cell of MCTS were observed in detail using a high-magnification 63× objective. The images clearly demonstrated that the micelles internalized into the cells and released drugs, and that the released drugs eventually accumulated in the cell nuclei (bar = 50 μm).

The Micelles Suppress Tumor Growth in Mice with Enhanced Therapeutic Efficacy and Lowered Toxicity. The animal tests revealed that the micelles exerted an effective antitumor activity over a broad range of injection doses to suppress tumor growth in mice, showing some of the clear comparisons with ADR (Figure 5). In the case of ADR, tumor growth was suppressed with a 10 mg/kg dose, but the mice treated with a 15 mg/kg dose were dead due to the drug's toxicity. This corresponds well to the fact that the lethal dose of ADR killing 50% of the test animals within a designated period, called LD_{50}, is generally 12.7−13.2 mg/kg. On the contrary, the micelles were safely injectable up to a 40 mg/kg dose, while three of six mice were completely cured and there was no death among the treated mice. Notably, the body weights of the mice that slightly decreased during the micelle administration recovered, or even increased, on day 30 with respect to the controls (Table 2). Such behavior was not observed in the case of ADR, and the mice were emaciated with a 10 mg/kg dose that was the optimum dose for ADR to suppress tumor growth. Namely, the therapeutic efficacy of the micelles was significantly improved over that of ADR within this animal experiment setting, which distinguishes the micelles from ADR that has a narrow therapeutic window between 10 and 15 mg/kg. In the meantime, the tumor-suppressing antitumor activity of the micelles is shown from a 20 mg/kg dose. The micelles also extended the duration of tumor growth reaching a 5-fold initial tumor volume up to 22 and 28 days for the 20 and 40 mg/kg doses, respectively. These results indicate that the micelles achieved both enhanced therapeutic efficacy and a reduced toxicity of the loaded drugs, which are of great advantage to create effective and safe drug carrier systems.

Table 2. In Vivo Antitumor Activity of the Micelles against C26 Tumor-Bearing Mice

sample	dose (mg/kg)[a]	body weight change on day 30 (%)[b]	toxic death	duration days of tumor growth[c]	complete cure
control	0	−2.18 ± 1.74	0/6	3.7	0/6
ADR	5	−13.35 ± 0.59	0/6	4.2	0/6
	10	−16.84 ± 1.26	0/6	14.6	1/6
	15	–	6/6	–	–
micelle	5	−0.89 ± 1.68	0/6	3.9	0/6
	10	−4.51 ± 1.44	0/6	4.0	0/6
	20	3.13 ± 1.60	0/6	22.1	2/6
	40	−4.07 ± 0.92	0/6	27.9	3/6
	60	–	6/6	–	–

[a] Administrations were carried out three times with a 4-day interval, and doses were determined in free ADR equivalents. [b] Body weights were measured on day 30 after the first injection to compare the long-term toxicity between ADR and the micelles. Values are expressed as mean ± SEM. [c] Duration time to reach 5-fold initial tumor volume.

The Micelles Circulate for a Long Time in the Blood and Selectively Accumulate in Solid Tumors. Effective antitumor activity and low toxicity imply that the micelles are stable in the blood without drug release (or leakage); therefore, their systemic and local distribution may dominate the tumor-suppressing antitumor activity. To demonstrate this, we investigated the in vivo dispositions of the micelles in detail using a biodistribution study. The levels of the micelles in the blood, tumor, and major organs, such as the heart, kidney, liver, and spleen, are expressed as percentage of each dose at specific times after the intravenous injection (Figure 6A). As summarized in Table 3, the micelles circulated in the blood for a prolonged time, and the area under the concentration curve (AUC) of the blood was 15-fold greater than that of ADR. In particular, it is noteworthy that the AUC values of the micelles in the heart and kidney decreased as compared to ADR, indicating that their tumor selectivity (AUC_{tumor}/AUC_{organ}) increased 6- and 5-fold higher with respect to the heart and the kidney, respectively. Such tumor-selective accumulation of the micelles may reduce the side effects of ADR such as cardiotoxicity and nephrotoxicity. In the meantime, the micelles showed a relatively low uptake in the liver and spleen despite the long residence time in the blood in comparison with tumors. These results suggest that the micelles may rapidly evacuate from these reticular

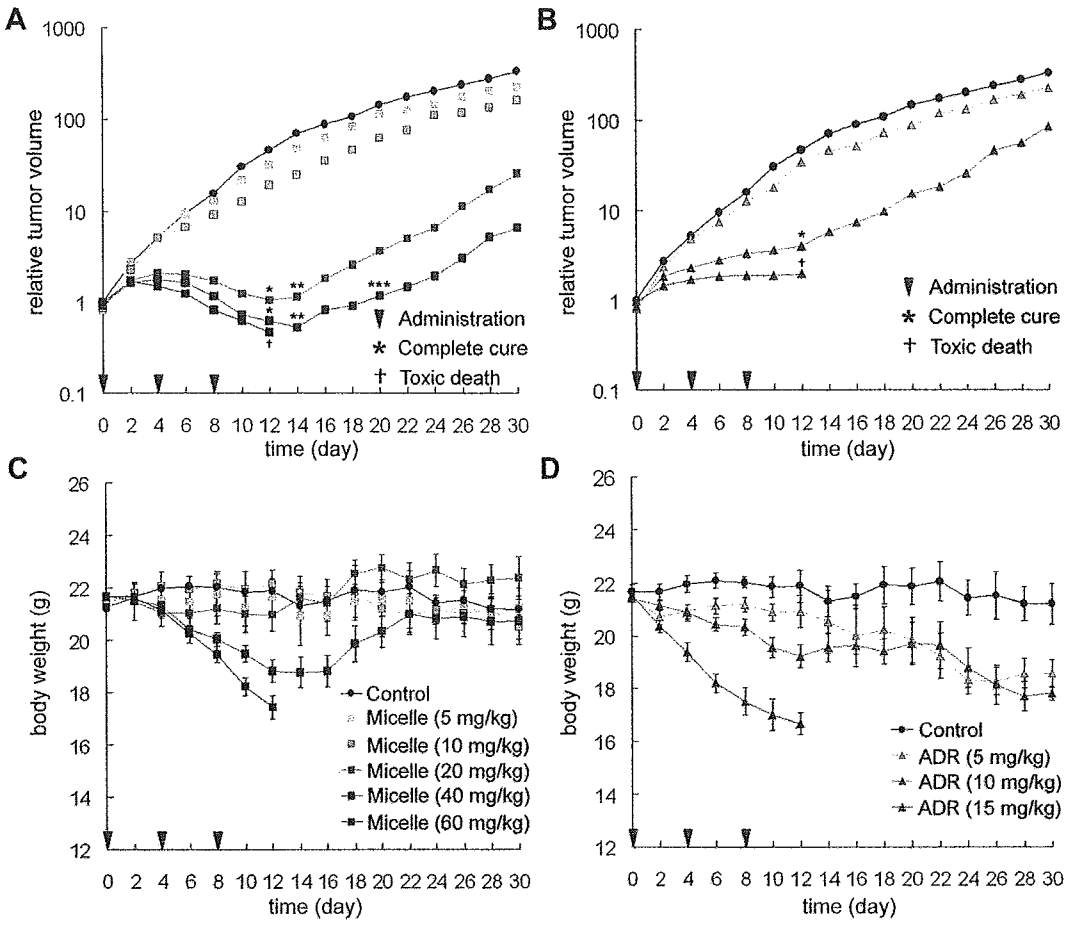

Figure 5. Tumor size and body weight changes of the treated mice. The figures show effective tumor-suppressing activity and low change in body weights over a broad range of injection doses of the micelles (A and C). To the contrary, ADR showed a narrow therapeutic window between 10 and 15 mg/kg does avoiding toxic death (B and D). Administrations were carried out three times with a 4-day interval into tumor bearing CDF1 mice (female, 6-week-old, $n = 6$). The micelle doses are shown as ADR equivalents. Values are expressed as mean and mean ± SEM for the tumor volume and body weight, respectively.

connective tissues without interacting with monocytes and macrophages that are responsible for engulfing and removing cellular debris, old cells, and unwelcome external invaders from the bloodstream. On the contrary, tumor tissues are characterized by a large vascular permeability and high interstitial diffusivity while a lack of lymphatic drainage is observed. This phenomenon is explained by the enhanced permeability and retention (EPR) effect, which significantly affects distributions of the macromolecules facilitating their access and accumulation in tumors (*30, 31*). Consequently, the micelles that accumulated in the solid tumors through the EPR effect can stay for a prolonged time. The biodistribution study, therefore, showed that the cytotoxicity of the micelles seems to depend on their retention time as well as in the accumulated amounts in each organ, which may be crucial in attaining both an effective antitumor activity and reduced toxicity in a single drug carrier system.

In vivo antitumor activity test showed that the micelles effectively suppressed tumor growth in mice over a broad range of injection doses while toxicity remained extremely low. On the other hand, the biodistribution study revealed that the micelles circulated in the blood for a long period of time and accumulated in normal organs as well as the tumors. These results are very interesting because the micelles showed organ-dependent differences in cytotoxicity. To elucidate this, we investigated the localization of the micelles in each organ by calculating the tissue-to-blood concentration ratio K_b (Table 4). The K_b value is defined as $[K_b = C_{tissue}/C_{blood}]$ where C_{tissue} and C_{blood} denote the tissue concentration and the blood concentration of the micelles, respectively. Each K_b value indicates distribution of the micelles in vascular space ($K_b < 0.1$), extracellular space ($0.1 < K_b < 0.5$), and intracellular space ($0.5 < K_b$) (*32, 33*). The data revealed that the micelles localized in the cell interior of tumor tissues but mainly distributed in the extracellular space of other organs after accumulation. It is in good accordance with our previous results published elsewhere (*34, 35*). We speculate that such drastic alterations might be due to the pathological differences in vasculatures and lymphatic drainages between organs. Consequently, even though the micelles accumulate in normal organs, they can be excreted from the body before releasing drugs. The organ-dependent cytotoxicity of the micelles, therefore, probably would depend on their retention time as well as the accumulated amounts in each organ.

The Micelles Regulate the Local Drug Distribution within Solid Tumors. In view of their tumor-specific accumulation and intracellular distribution, the micelles should release the drugs in solid tumors along with emitting fluorescence as we observed in the intracellular drug release experiment using MCTS. In contrast, if the micelles released the drugs slowly or not at all, the fluorescence of ADR would remain quenched. On the basis of this hypothesis, we observed the solid tumors and their peripheral blood vessels in mice after intravenous injection of the micelles using a fluorescence microscope (Figure 6B). The observations were carried out at 24 h after injection because the micelles needed to

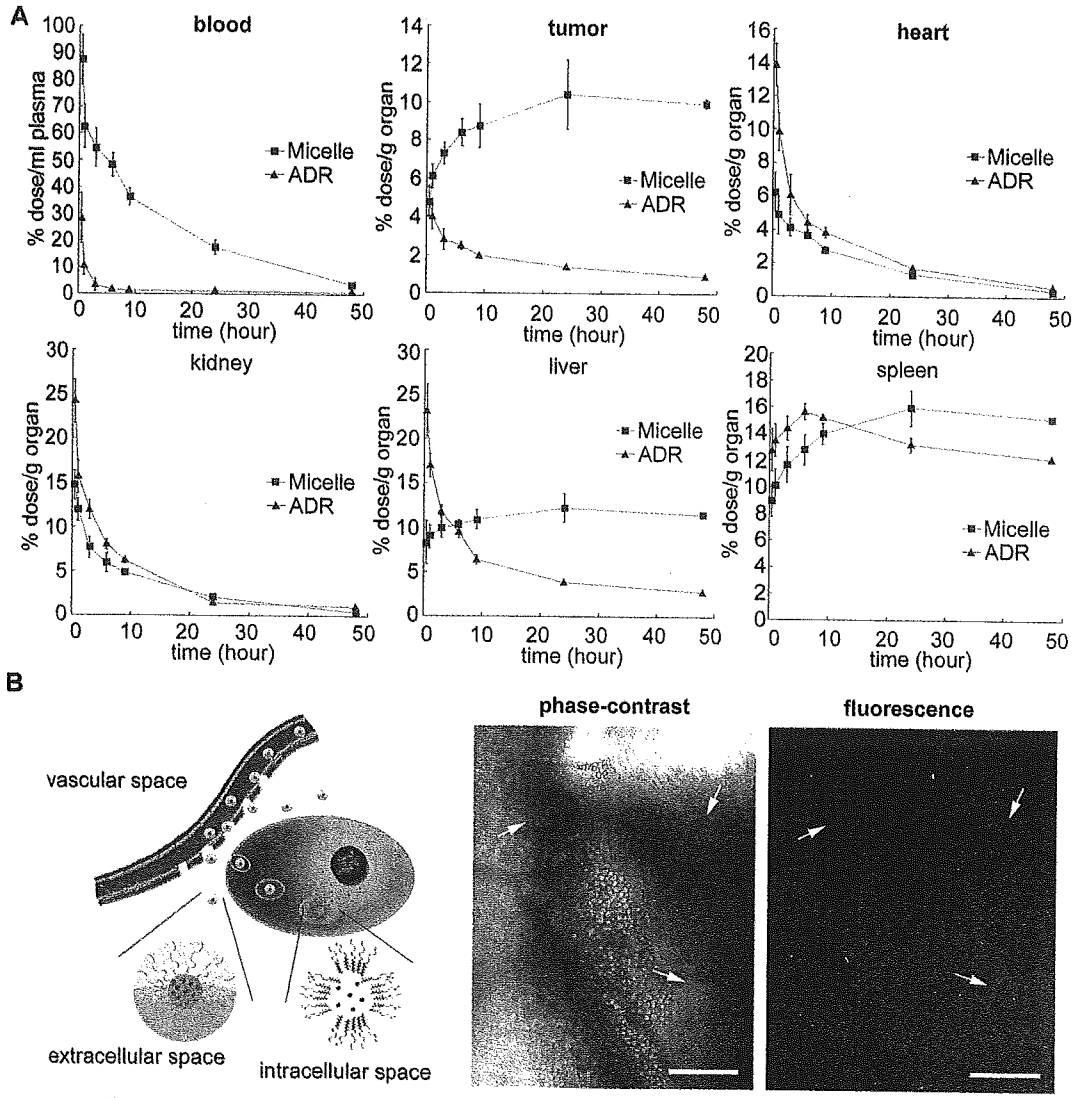

Figure 6. Tumor-specific accumulation of the micelles and locally increased drug concentrations. (A) Biodistribution study revealed the prolonged circulation in the blood and tumor-specific accumulation of the micelles. (B) Fluorescence microscopic observations of the solid tumor and its peripheral regions at 24 h after micelle injection demonstrate that the drug concentrations in the tumor tissues selectively increased due to the tumor-specific accumulation and controlled drug release from the micelles (bar = 500 μm).

Table 3. Tumor-Specific Accumulation of the Micelles

	AUC[a]		AUC ratio ($AUC_{micelle}/AUC_{ADR}$)	tumor selectivity[b] (AUC_{tumor}/AUC_{organ})		tumor selectivity ratio [$(AUC_{tumor}/AUC_{organ})_{micelle}/(AUC_{tumor}/AUC_{organ})_{ADR}$]
	ADR	micelle		ADR	micelle	
blood	58.86	858.54	14.59	–	–	–
tumor	49.59	210.21	4.24	–	–	–
heart	94.70	65.24	0.69	0.52	3.22	6.19
kidney	151.56	117.80	0.78	0.33	1.78	5.39
liver	176.15	261.17	1.48	0.28	0.80	2.86
spleen	341.38	329.66	0.97	0.15	0.64	4.27

[a] AUC denotes the area under a concentration curve that is obtained from the biodistribution study. Values are calculated based on the trapezoidal rule up to 24 h after intravenous injection. [b] Tumor selectivity of ADR and the micelles was determined by calculating the relative accumulated concentrations between the tumor tissues and each organ (AUC_{tumor}/AUC_{organ}). Their ratios indicate the change in the tumor selectivity of the micelles with respect to ADR.

accumulate in the tumor tissues enter the cells and release the drugs intracellularly as long as they were present in the blood. A phase-contrast image showed that the tumor blood vessels containing the micelles begin to leak into the extravascular compartment of the solid tumors (note the red color of the micelles). However, no fluorescence was detected at the corresponding part but in the limited regions of the solid tumor. Therefore, even though colloidal drug carriers are generally considered to localize in the limited peripheral regions of the solid tumors due to poor accessibility, we have confirmed that the micelles can infiltrate into tumor tissues after accumulation, thus increasing the local drug concentration. This conclusion is in good accordance with the results from the permeability testing of the micelles into MCTS.

DISCUSSION

This paper has revealed a new potency of the polymeric micelle drug carrier systems that they can directly deliver drugs to the interior of targeted cells in vivo by infiltrat-

Table 4. Tissue-to-blood Concentration Ratio (K_b) in Each Organ[a]

	organ				
time (h)	tumor	heart	kidney	liver	spleen
0.5	0.0545	0.0714	0.168	0.0946	0.1023
1	0.0976	0.0772	0.1903	0.1429	0.1617
3	0.134	0.0755	0.1402	0.1834	0.2136
6	0.1747	0.0764	0.1226	0.2141	0.2651
9	0.2412	0.0762	0.134	0.3014	0.3859
24	0.5992	0.0761	0.1162	0.7037	0.9158

[a] K_b value is defined as $[K_b = C_{tissue}/C_{blood}]$ where C_{tissue} and C_{blood} were the tissue concentration and the blood concentration of the micelles, respectively. Each K_b value indicates the distribution of the drugs in vascular space ($K_b < 0.1$), extracellular space ($0.1 < K_b < 0.5$), and intracellular space ($0.5 < K_b$).

ing into solid tumors. These findings provided a clear answer to the questions whether the nanosized supramolecular drug carriers can access the cells in the avascular region of the solid tumors without structural and functional breakdown, which is also crucial to other intracellular environment-sensitive macromolecular bioconjugates that are injected through the vein for tumor targeting.

For the past several decades, natural and artificial macromolecules have evolved into a very useful class of drug delivery media (*36*–*39*). However, their in vivo applications are not always successful because limited accessibility inside solid tumors causes stagnation of drug carriers at the periphery of the tumor vasculatures, inducing low concentrations of active drugs in the targeted tumor tissues (*40*). Such a poor delivery efficiency of active drugs to the solid tumors is considered a serious problem facing recent cancer therapy using drug carriers. In this regard, we considered that the intrinsic characteristics of drug carriers may play a critical role in determining their in vivo behaviors, such as tumor permeability, drug release property, and antitumor activity. To confirm this, a suitable carrier model is required that controls the release of drugs while its structural features are optimized for a tumor-targeting drug delivery, and we prepared a new type of drug carrier in this study by adding an intracellular pH-triggered drug release property to the polymeric micelle drug carrier system whose chemical and biological properties are clearly identified (*41*).

As shown in the experimental results, the prepared micelle behaves not only as a biocompatible nanosized drug carrier with a high drug-loading content but also as a bioresponsive device with intracellular pH-sensitivity to control the drug release. These characteristic behaviors suggest that the nanosized core–shell structure of the micelles seems important to take the best advantage of the PEG shielding, imparting both stability and fragility into a single carrier system. The micelles safely protect the loaded drugs and functional linkers by providing a nanocompartment in the core that is completely segregated from the external environments; they maintain a high water-solubility with the hydrophilic shell that prevents the adsorption of proteins and the adhesion of cells so as to circumvent the uptake by reticuloendothelial systems during blood circulation (*42*, *43*). In the meantime, intracellular trafficking of the micelles in the solid tumors is evident, which indicates that PEG shielding of the micelle may behave as a kinetic barrier that regulates the condition of the molecular affinity interaction between the micelles and cell membrane according to the exposure or retention time. As explained by the EPR effect, solid tumors feature a large vascular permeability, high interstitial diffusivity, and poor lymphatic drainage; this is a fact that results in tumor-specific retention over a long period of time required for interacting with tumor cells. The retention time in each organ influences the intracellular trafficking of the micelles; thereby, any undesirable cytotoxicity to the normal organs is avoided. Consequently, the intracellular pH-triggered drug release property of the micelles should be the major reason for in vivo antitumor activity with low toxicity.

In conclusion, the intracellular pH-sensitive polymeric micelles exemplify the supramolecular drug carriers that control the systemic, local, and subcellular distribution of the active drugs. They show a higher bioavailability than free drugs, and therefore, the intracellular delivery of drugs would be the most effective and promising formulation for cancer chemotherapy with enhanced therapeutic efficacy and low toxicity. Moreover, the study reveals that the biocompatible structure and environment-sensitive functionality should be considered as a single event in order to realize the carrier systems that are related to these intracellular environments and material transports for the future treatment of cancers with avascular tumor tissue.

ACKNOWLEDGMENT

This research was supported by a Grant-in-Aid for Scientific Research from the Ministry of Education, Culture, Sports, Science and Technology (MEXT), Japan, and by Core Research for Evolutional Science and Technology (CREST), Japan Science and Technology Corporation (JST).

Supporting Information Available: Synthetic scheme for PEG-p(Asp-Hyd-ADR) block copolymer. HPLC analysis protocol for biodistribution. This material is available free of charge via the Internet at http://pubs.acs.org.

LITERATURE CITED

(1) Duncan, R. (2003) The dawning era of polymer therapeutics. *Nat. Rev. Drug Discovery 2*, 347–360.

(2) Maeda, H. (2001) SMANCS and polymer-conjugated macromolecular drugs advantages in cancer chemotherapy. *Adv. Drug Delivery Rev. 46*, 169–185.

(3) Jain, R. K. (2001) Delivery of molecular and cellular medicine to solid tumors. *Adv. Drug Delivery Rev. 46*, 149–168.

(4) Kopecek, J. (2003) Smart and genetically engineered biomaterials and drug delivery systems. *Eur. J. Pharm. Sci. 20*, 1–16.

(5) Nishiyama, N., Okazaki, S., Cabral, H., Miyamoto, M., Kato, Y., Sugiyama, Y., Nishio, K. Matsumura, Y., and Kataoka, K. (2003) Novel cisplatin-incorporated polymeric micelles can eradicate solid tumors in mice. *Cancer Res. 63*, 8977–8983.

(6) Lewanski, C. R. I., and Stewart, S. (1999) PEGylated liposomal adriamycin: a review of current and future applications. *Pharm. Sci. Technol. Today 2*, 473–477.

(7) Jensen, K. D., Nori, A., Tijerina, M., Kopeckova, P., and Kopecek, J. (2003) Cytoplasmic delivery and nuclear targeting of synthetic macromolecules. *J. Controlled Release 87*, 89–105.

(8) Lian, T., and Ho, R. J. Y. (2001) Trends and developments in liposome drug delivery systems. *J. Pharm. Sci. 90*, 667–680.

(9) Kataoka, K., Kwon, G., Yokoyama, M., Okano, T., and Sakurai, Y. (1993) Block-copolymer micelles as vehicles for drug delivery. *J. Controlled Release 24*, 119–132.

(10) Ringsdorf, H. (1975) Structure and properties of pharmacologically active polymers. *J. Polym. Sci. Polym. Symp. 51*, 135–153.